**PHD DISSERTATION**

# A Long-Period Grating Sensor for Wind Turbine Blades

by Lars Glavind

AARHUS
UNIVERSITY

# A Long-Period Grating Sensor for Wind Turbine Blades

# A Long-Period Grating Sensor for Wind Turbine Blades

**PhD Thesis by**

**Lars Glavind**

*Aarhus University Department of Engineering, Denmark*

AARHUS
UNIVERSITY
DEPARTMENT OF ENGINEERING

River Publishers

ISBN 978-87-93102-89-7 (e-book)

*Published, sold and distributed by*:
River Publishers
P.O. Box 1657
Algade 42
9000 Aalborg
Denmark

Tel.: +45369953197
www.riverpublishers.com

# Abstract

This PhD project, “A Long-Period Grating Sensor for Wind Turbine Blades”, has been carried out in collaboration between Vestas Wind Systems A/S and Aarhus University, Denmark, together with partners at The University of Sydney and The University of New South Wales, Australia. The work presented in this PhD thesis concerns applied research in the field of fibre optical load sensors for structural health monitoring of wind turbines blades. Moreover, it concerns the applied research for providing a novel sensor for measurements based on Long-Period Gratings.

The idea is based on the utilization of a special asymmetrical optical fibre with a Long-Period Grating for directional sensitive bend sensing. The project involves the processes from feasibility study of fibre grating technology to the embedding and test on a full scale wind turbine blade. The project has involved the design and manufacturing of a D-shape optical fibre. Writing of Long-Period Gratings, into the D-shape fibre, in Mach Zehnder configuration, to optimize the directional sensitivity and the resolution. The project includes the process of embedding the optical fibre directly into the wind turbine blade material, where a suitable process and recoating material were investigated. The sensor was implemented and tested on a full scale wind turbine blade placed on a test rig.

This first prototype of this novel sensor has demonstrated the capability of the sensor for wind turbine blade monitoring, particular the possibility to distinguish between the flap- and edge-wise bend directions on the wind turbine blade, providing a selective sensor. The sensor has proven to be very robust and suitable for this application.

# Resumé

Dette PhD project, "En Lang-Periodisk Gitter Sensor for Windmølle Vinger", er blevet udført I samarbejde imellem Vestas Wind Systems A/S og Aarhus Universitet, Danmark, sammen med partnere ved The University of Sydney og The University of New South Wales, Australien. Det præsenterede arbejde in denne PhD afhandling omhandler anvendt forskning inden for området fiber optiske last-sensorer for overvågning af vindmølle vingernes tilstand. Nærmere betegnet, det omhandler anvendt forskning for at fremkomme med en ny sensor for disse målinger, baseret på Lang-periodiske gittre.

Ideen er baseret på anvendelse af specielle asymmetriske optiske fibre med Lang-Periodiske Gittre for retnings følsom bøjnings sensore. Projektet involverer muligheds-undersøgelse af fiber teknologi til indstøbning og test på en fuld skala vindmølle vinge. Projektet har involveret design og fremstilling af en D-formet optisk fiber. Skrivning af Lang-Periodiske Gittre, i den D-formede fiber, i en Mach Zehnder konfiguration, for at optimere retnings-følsomheden og opløsningen. Projektet indeholder processen af at indstøbe den optiske fiber direkte i vindmølle vinge materialet, og en passende proces og gen-coating materiale er undersøgt. Sensoren var implementeret og testet på en fuld skala vindmølle vinge, som var placeret på en test-stand.

Denne første prototype af den ny type sensor har demonstreret kapabilitet af sensoren for målinger på vindmølle vinger, specielt muligheden for at skelne imellem flap- og kant-vis bøjnings retning på en vindmølle vinge, givende en selektiv sensor. Sensoren har vist at være yderst robust og anvendelig for denne applikation.

## Acknowledgement

First of all the author would like to thank his supervisors at Aarhus University Martin Kristensen and Bjarne F. Skipper for introduction to the field, initiating the project and also for all help and inspiration during my studies, this has been essential. I would also like to thank John Canning and Gang-Ding Peng for great help and for support with fibre facilities, during my stays in Sydney. I also thank Kevin Cook, Shaorui Gao and Yanhua Luo for their help in the labs during fibre fabrication and writing of gratings.

At Vestas I would like to thank all my colleagues. Especially I would like to thank Morten Thøgersen for establishing the project and for his guides during the project. I would also like to thank Ib S. Olesen for idea generation and support. For discussions, help with embedding, testing and proofreading I would like to thank Stephen Buggy. I also thank manager Niels Juul for good support during the project.

I would like to thank Aarhus University and Vestas Wind Systems A/S for providing me the opportunity to write a PhD thesis in their respective departments.

Dedicate to my family.

# Content

# Publication List

### Journals

**L. Glavind**, I. S. Olesen, B. F. Skipper, and M. Kristensen, "Fibre-optical grating sensors for wind turbine blades: a review," *Optical Engineering 52*, 030901-1 - 030901-9 (2013).

J. Canning, L. Moura, L. Lindoy, K. Cook, M. J. Crossley, Y. Luo, G. D. Peng, **L. Glavind**, G. Huyang, M. Naqshbandi, M. Kristensen, C. Martelli and G. Town, "Fabricating Nanoporous Silica Structure on D-Fibres through Room Temperature Self-Assembly", *Materials* 7, 2356-2369 (2014).

**L. Glavind**, J. Canning, S. Gao, K. Cook, G.D. Peng, Y. Luo, B. F. Skipper and M. Kristensen. "Long-Period Gratings in Special Geometry Fibres for High Resolution and Selective Sensors", *Optical Engineering*, (submitted Jan. 2014)

**L. Glavind**, S. Buggy, J. Canning, S. Gao, K. Cook, Y. Luo, G.D. Peng, B. F. Skipper and M. Kristensen. "Long-Period Gratings for Selective Monitoring of Loads on a Wind Turbine Blade", *Applied Optics,* (Submitted Mar. 2014).

### Conferences

**L. Glavind**, S. Buggy, I. Olesen, B. Skipper, J. Canning, K. Cook, and M. Kristensen, "Direct Embedding of Fibre-Optical Load Sensors into Wind Turbine Blades," in *Advanced Photonics 2013, OSA Technical Digest*, paper SM3C.6 (2013).

**L. Glavind**, S. Gao, K. Cook, J. Canning, B. F. Skipper, Y. Luo, G. Peng and M. Kristensen, "Enhanced resolution of Long-Period Grating bend sensor", *Proc. SPIE 8924, Fourth Asia Pacific Optical Sensors Conference*, 892437 (2013).

**L. Glavind**, I. Olesen, M. Thøgersen, B. Skipper, and M. Kristensen, "Low-Cost, High-Resolution Strain Sensor for Wind Turbine Applications," in *Advanced Photonics & Renewable Energy*, *OSA Technical Digest*, paper JThA36, (2010).

L. Moura, J. Canning, L. Lindoy, K. Cook, M. Crossley, Y. Luo, G. Peng, **L. Glavind** and M. Kristensen, "A fluorescence study of self-assembled silica layers on D-shaped optical fibre", *Proc. SPIE 8924*, *Fourth Asia Pacific Optical Sensors Conference*, 89241V (2013).

J. Canning, L. Lindoy, G. Huyang, M. Naqshbandi, K. Cook, M. Crossley, Y. Luo, G. Peng, **L. Glavind,** and M. Kristensen, "Exploring the room temperature self-assembly of silica nanoparticle layers on optical fibres ". *Proc. SPIE 8793, Fourth International Conference on Smart Materials and Nanotechnology in Engineering,* 87930J, (2013).

J. Canning, L. Lindoy, G. Huyang, M. Naqshbandi, K. Cook, M. Crossley, Y. Luo, G. Peng, **L. Glavind**, G. Town, and M. Kristensen, "RT Self-assembly of Silica Nanoparticles on Optical Fibres," in *Workshop on Specialty Optical Fibres and their Applications*, paper F2.3, (2013).

**L. Glavind**, S. Buggy, B. F. Skipper, J. Canning, S. Gao, K. Cook, Y. Luo, G. Peng and M. Kristensen, "A Long-Period Grating Sensor System Monitoring Loads on a Wind Turbine Blade," in *Bragg Gratings, Photosensitivity and Poling in Glass Waveguides* (BGPP), (Submitted Jan. 2014).

**L. Glavind**, J. Canning, S. Gao, K. Cook, G. Peng, Y. Luo, B. F. Skipper and M. Kristensen, "D-shape fiber with Mach Zehnder Long-Period Gratings For a High Resolution and Selective Sensor," in *Bragg Gratings, Photosensitivity and Poling in Glass Waveguides* (BGPP), (Submitted Jan. 2014).

**Patent applications**

**L. Glavind**, I. S. Olesen, M. Hancock and R. Craven, "System and method for detecting damage to a wind turbine blade". WO2012110041, (2012).

I. S. Olesen and **L. Glavind**, "System and Method for Identifying the Likelihood of a Tower Strike where a Rotor Blade Strikes the Tower of a Wind Turbine", US 20130287567 A1, (2010).

# 1. Introduction

The renewable energy industry is undergoing a period of extensive development and wind turbines have seen a rapid development in their size and complexity over the last decade. Modern wind turbines generate megawatts of power and have rotor diameters that are in excess of 150 m. This recent development in size has refocused the industry's efforts on condition-monitoring of wind turbine components to reduce failure and maintenance costs. The majority of this effort has been on active optimization of wind turbines, based on structural-monitoring of loads on wind turbine blades [1]. One method is to utilize sensors directly embedded into the blade, providing data and information about strain or curvature of the blade. Combined with individual pitch-control technology of the wind turbine blades, the loads on the blades and on the drive-train, can be actively optimized without exceeding the safe limit, to prolong the operating lifetime [1]. An added incentive is the possibility to reduce the build-cost of the turbine. Furthermore, with utilization of condition-monitoring of blades, it might be possible to see changes in movement pattern of the blades, and thereby predict which blades that are likely to become damaged, before a critical fatigue failure occur, such as the one shown in figure 1.

Figure 1 – Wind turbine with a critical blade failure, from [2]

A "cost-benefit" report from 2002, performed by Risø DTU National Laboratory for Sustainable Energy [3], regarding load sensors and with focus on damaged and down-time cost for wind turbines concluded that such a sensor system will have a cost break-even time of 3 to 8 years depending on the cost of the sensor system [3].

Optimization based on pitching the blades with feedback information from embedded sensors, providing reduction of weight and increased power production, are not included in the "cost-benefit" report, and this can only reinforce the business-case. Furthermore, the report is 10 years old, and the size and weight has as mentioned increased significantly. Nevertheless, the report lays the foundation that it is possible to develop profitable structural health monitoring system in wind turbines.

For sensing in wind turbine blades, sensors based on fibre-optics is of particular interest. Compared to conventional electrical sensors, strain-gauges, fibre-optical sensors provide a number of advantages. A standard optical fibre has a diameter of 125 μm, without coating, and therefore lends itself well to direct embedding with a low risk of delamination [4]. There is also the possibility for multi-point sensors in the same fibre. Silica glass fibre has excellent material compatibility for embedding within glass-fibre wind turbine blades [5]. Furthermore, due to the high risk of lightning strikes on wind turbine blades fibre-optical sensors offer an added benefit being non-conductive and immune to electrical interferences. They have a significantly reduced risk of corrosion, and are thereby more robust than typical electrical sensors. However, there are some disadvantages with fibre-optical sensors such as thermal sensitivity, a limited number of suppliers and relatively high cost [6]. As the signal is confined in low-loss optical fibre, signal reception and signal processing can be conducted remote from the sensor, so any electrical parts in the wind turbine blade is avoided. In a wind turbine, there are lightning-protected environments in the Hub (the part of the structure where the wind turbine blades and the main shaft are connected), where electronic devices are housed. The data transfer between the rotating and the stationary part of a wind turbine typically through Fibre Optic Rotary Joints (FORJ), has been demonstrated for blade load sensing [7]. Wireless transmission has also been demonstrated between the signal processing unit in the wind turbine rotor and the data handling system in the nacelle has been demonstrated [8].

The potential for creating sensors within optical fibres has advanced since the discovery of photosensitivity in optical fibres in 1978 by Hill *et al.* [3]. For wind turbine applications, fibre gratings are of particular interest, with the two important technologies fibre Bragg gratings (FBGs) and Long-Period Gratings (LPGs). Fibre-optical gratings typically transform a sensed parameter, e.g. strain or temperature to wavelengths, and therefore have the advantage of being

independent of light levels, e.g. due to connector loss or changes in power from the light source.

FBG systems have been demonstrated in field tests on wind turbines, e.g. Schroeder *et al.* [9]. Several companies such as Moog [10], Fibresensing [11], Smartfibres [12] and HBM [13] provide commercial FBG sensing systems for wind turbine blade applications. Moreover subcontractors, such as these, holds patents for the applications on utilization structural monitoring with FBG technology on wind turbine blades [14, 15] and a novel competitive sensor would be advantages [16].

## 1.1 Preface and Thesis Content

This PhD project, "A Long-Period Grating Sensor for Wind Turbine Blades", has been carried out in collaboration between Vestas Wind Systems A/S and Aarhus University, Denmark, and together with partners at The University of Sydney and The University of New South Wales, Australia. The project was initiated on the background of limited freedom to operate with FBG strain sensors and on the possibility of using asymmetrical fibres with a LPG for bend sensing [17]. This project involves the processes from feasibility study of fibre grating technology, to design, manufacturing, embedding, implementing and testing on a full scale wind turbine blade. The approach has partly been applied research with experiential work to establish knowledge regarding the capability of the sensor and to identify issues and uncertainties. The aim of this research project is to demonstrate proof of principle/concept with a sensor based on LPGs in special fibres, implemented on a full scale wind turbine blade, providing the foundation for a decision of a development project for commercialization of the sensor device.

The content of this thesis is as follows. In chapter 2 a description of the theory of gratings in the aspect of wind turbine blade load sensors is provided with an overview of the state of art in this field. The work this thesis is based on is divided into two chapters, 3 and 4 respectively, the first part presents the design and fabrication of sensors, and the second part presents the embedding and testing of the sensor.

# 2. Fibre Gratings

In this chapter a survey of the grating technology, particularly FBG and LPG is presented. The chapter is mainly based on the work presented in the publication "Fibre-optical grating sensors for wind turbine blades: a review" [18]. This paper provides review of this field and describes the current status of utilization fibre optical gratings technology as wind turbine blade load sensors.

## 2.1 Fibre Bragg Gratings

### Introduction

An optical fibre consists of a core, $n_2$, and a cladding, $n_1$, typically silica and with germanium doping of the core to increase the refractive index (RI) to guide light along the fibre. A fibre optical grating consists of a periodic modulation of the properties of an optical fibre, typically changes in the RI of the core, $n_3$. With the right phase conditions a given wavelength is reflected and all others transmitted, see figure 2. A considerable amount of literature has been published regarding FBGs [19-25].

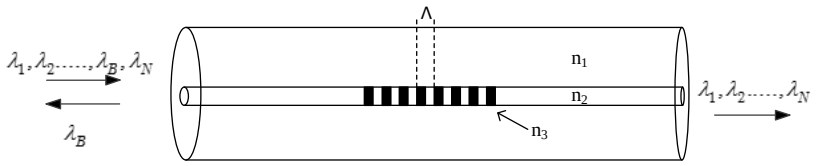


Figure 2 – Illustration of reflected light from an FBG

The discovery of light-induced RI changes in silica glass has been attributed to Hill *et al.* [26] in 1978. An intense Argon-ion laser was launched in a fibre; and due to the standing wave intensity pattern from the Fresnel reflection a grating along

the fibre was photo-induced. However the grating is limited to the spatial periodicity of the interference pattern. In 1989 Meltz *et al.* [27] demonstrated the transverse writing of Bragg gratings, utilizing an amplitude-splitting interferometer which produced an interference-pattern along the photosensitive fibre. The major advantage of this technique is the possibility to change the spatial periodicity by changing the angle of the beams. Today a phase-mask based side-writing with UV-illumination is normally the preferred production method for FBGs [28], see figure 3, as it provides a much more stable setup and is better suited to mass production. The phase-mask is made of silica glass with a surface relief structure with a periodic pattern. It is a diffractive optical element that spatially modulates the UV writing beam. Interference between the diffracted plus and minus first orders results in a periodic, near-field, high-contrast intensity pattern, having half the period of the phase mask grating period [22].

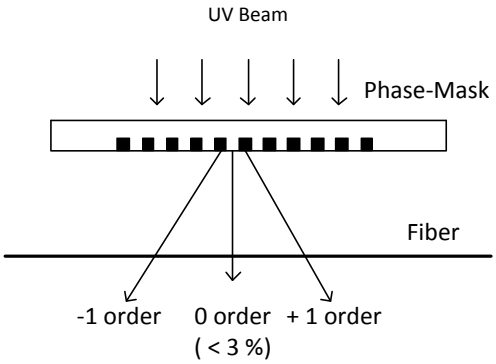


Figure 3 – Illustration of a phase-mask

The change in the RI is typically in the range of up to $1 \cdot 10^{-3}$ [22]. Germanium-doped fibre is most often used for inscribing FBGs, due to its ability to significantly increase the RI [29]. Boron can be co-doped to lower the RI, allowing higher concentrations of germanium in the core, to match standard telecommunications fibre while making the fibre highly photosensitive [30]. To increase the photosensitivity of fibres, they can also be loaded with hydrogen [31].

Wavelengths of light that impinge on the FBG that satisfy the Bragg condition will be reflected. If the Bragg condition is not satisfied, the reflected light from

each of the subsequent planes gradually become out of phase and will eventually cancel out. The first order Bragg wavelength is given by [22]:

$$\lambda_B = 2n_{eff}\Lambda \tag{1}$$

Where $\lambda_B$ is the Bragg wavelength, $n_{eff}$ is the effective RI of the fundamental mode and $\Lambda$ is the spatial period of the grating. In the 1500 nm range the grating-period is typically around 500 nm. FBGs typically have a total length about 5 mm [32].

Figure 4 shows a measured reflection spectrum of a commercially available FBG, with a centre-wavelength at 1551 nm and a Full Width at Half Maximum (FWHM) of 0.2 nm, typical FWHM for the reflected peak of an FBG sensor is typically between 0.05 nm to 0.3 nm [25]. Due to the short FWHM a larger number of FBGs can be written in the same fibre at different wavelengths and interrogated at the same time.

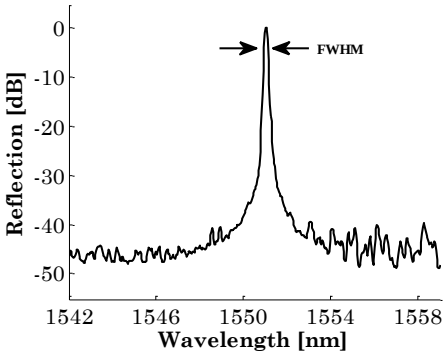


Figure 4 – Normalized reflection spectrum from a FBG, from [18]

**Temperature and Strain Sensitivity**

FBGs are sensitive to both temperature and strain due to changes in the material and the RI given the potential for utilization as sensors for innumerable applications. The applied strain or temperature causes the centre wavelength of the FBG to change and can thereby be interrogated. However the number of

consecutive FBGs along the same optical fibre will be limited by the grating FWHM, the induced strain and temperature wavelength tuning and the interrogator.

The strain sensitivity of FBGs depends of the fibre composition and the applied strain and is given by [22]:

$$\Delta\lambda_B = (1 - p_e) \cdot \lambda_B \varepsilon \tag{2}$$

Where $\Delta\lambda_B$ is the change in Bragg wavelength, $p_e$ is an effective strain-constant based on the strain-optic tensor and Poisson's ratio (change in transverse dimensions), with a typical value of 0.21 [22], $\lambda_B$ is the given Bragg wavelength and $\varepsilon$ is the applied strain. For small longitudinal deformations ($\delta << L_0$) the strain is defined as $\varepsilon = \delta / L_0$, where $\delta$ is the change in length, and $L_0$ is original length [33]. For a change in strain of 1 μm the wavelength shift will be about 1.2 μm in the 1500 nm range.

The temperature sensitivity of FBGs depends on the thermal expansion coefficient and the change in RI and is given by [22, 34]:

$$\Delta\lambda_B = \lambda_B \left(\alpha + \xi\right) \Delta T \tag{3}$$

Where $\alpha$ is the thermal expansion coefficient of the fibre, typically $0.55 \cdot 10^{-6}$ m/(m·K), and $\xi$ is the thermo-optic coefficient of the RI of the fibre, typically $8.6 \cdot 10^{-6}$ $K^{-1}$ [22]. For a typical 1550 nm FBG this corresponds to a shift of about 13.7 pm/K [22]. Within the typical sensing interval 233 K to 353 K (-40 °C to 80 °C) the thermo-optic coefficient can be assumed linear.

For strain sensing the cross sensitivity to temperature can be reduced by utilizing material with opposite thermal expansion, such as Zirconium Tungstate [35], for embedding. It is also possible to exploit the temperature-sensitivity of FBGs and actually measure the temperature with an additional, mechanically decoupled, FBG and utilize it to actively compensate for temperature drift in the control-software.

**Fibre Bragg Gratings for Sensing on Wind Turbine Blades**

FBG based strain measurement on wind turbines for load monitoring has been demonstrated in several papers [1, 4, 8, 9, 36-39]. The sensor-systems reported are capable of providing a resolution of 1 με with a dynamic range of ±5000 με for structural information systems on wind turbine blades. Typically 2-6 sensors are required for control applications and 8-16 sensors for supervision applications. FBGs allow for these applications to be supported in one measurement channel because multiple (tens to hundreds) FBG sensors can be inscribed in a single optical fibre. A typical application for wind turbines is in the measurement of strain in the root, where the sensors are placed in the circumference of the blade-root, and the sensors are orientated in the longitudinal direction. By mounting more than one sensor cylindrically in the wind turbine blade, the sensors can also provide edge wise and flap wise strain sensing.

FBGs have been compared to standard electrical strain-gauges on a small scale wind turbine blade [1]. The experiment demonstrated that the Fourier spectrum of the strain-gauges and the FBGs was similar. However, more resonance peaks were found in the Fourier spectrum of the FBGs. This illustrates the potential for the application of FBGs as a method to capture the different resonance-modes of the wind turbine blades. Furthermore, research studies regarding FBG utilized as impact response sensors on wind turbine blades have also been published [5].

Wind turbines have a requirement of 20 years' operating lifetime [9], and therefore are comparable with the requirements given to components that are not able to be maintained (repaired). Therefore the aspect of embedding the sensors in wind turbine blades is very important. Krebber *et al.* [4] demonstrated embedded FBG sensors in composite structures for wind turbine blades, but concluded that more research is required regarding an optimized coating to provide reliable measurement results over the lifetime. Furthermore, the grating reflectivity decays over time, however, it is possible to slow down the decay by an annealing treatment and ensure a lifetime of the required 20 years [40]. Optical fibres have a median breaking strain of 57.000 με, much larger than the maximum strain of about 5.000 με a sensor would force on a wind turbine blade. The UV exposure during writing gratings reduces the breaking point to about to 27.000 με after UV exposure during writing of FBGs [41]. Moreover the optical fibre sensor still has a breaking strength sufficiently higher that the maximum strain a sensor would be subject to. Great care must be taken to avoid microscopic scratches/cracks in the

fibre during cladding-stripping and re-coating/gluing process to ensure a robust sensor is resultant. Alternative manufacturing methods by FBG suppliers, e.g. FBGS-technologies, [42] provide FBGs that are written during production of the optical fibre. This provides more robust fibres since the fibre is homogeneously coated and this decreases the possibility of a defect sensor due to tiny cracks from the removing of coating and imperfect re-coating.

FBG sensor systems suitable for wind turbine blade load sensing have been commercialised and several companies such as Moog [10], Fibresensing [11], Smartfibres [12] and HBM [13] provide industrial FBG sensing products where the sensors are typically embedded on the inside surface of the wind turbine blade. These commercial systems normally offer resolutions down to 1 με with a typical dynamic range up to ±5000 με.

The detection systems for FBGs are relatively expensive, since a wavelength range of up to 50 nm, with a resolution in the range of 1 pm, needs to be interrogated. This is most easily achieved with a tunable narrow-band source and a photo-diode or a combination of a broadband light source and a spectrometer. However companies such as Redondo Optics [43], provides cheaper solutions based on WDM filters (Wavelength Division (de)-Multiplexing) in integrated optics. The systems are typically more limited in resolution, dynamic range and number of sensors. However this detection technique has also been demonstrated to meet high resolution demand for use in wind turbine applications [44].

Another possibility to measure the loads on a wind turbine blade is the utilization of a sensor that is capable of measuring the curvature of the wind turbine blade. Strain on the wind turbine blade is the result of stresses imparted on the blade largely by the interaction of the wind on the aerofoil shape. This interaction also forces the wind turbine blades to bend. Therefore it might be better to measure the curvature of the wind turbine blade directly. FBGs have also been demonstrated as bending sensors with a sensitivity of $0.77 \cdot 10^{-12}$ $m^2$ [45]. However this has not been implemented in wind turbine applications, and there are some uncertainties in its deployment as such a sensor, e.g. resolution requirements. Bend sensors in polymer optical fibres based on FBGs have been demonstrated by Chen *et al.* [46, 47]. However, polymer optical fibres are more fragile and sensitive to mechanical exhaustion than typical silica optical fibres, and therefore they are not preferred for applications in wind turbines.

### Discussion

FBG strain sensors for structural monitoring on wind turbine blades is a mature and highly developed technology that can more than fulfil the requirements for blade sensors, such as immunity to lightning, long lifetime and the necessary resolution and sensitivity. The concept has been demonstrated in field tests, and FBG strain sensing systems specific for wind turbine applications are commercially available. However as mentioned in chapter 1, the utilization of FBGs on wind turbines is a heavily patented field, with very limited freedom to operate for wind turbine manufactures, therefore an alternative technology might be advantageous.

## 2.2 Long-Period Gratings

### Introduction

Another type of grating technology is LPGs. As the name indicate the period of the grating is longer than those more typical of FBGs, LPGs have spatial periods in the range of 100-500 μm, which is approximately a factor 1000 times larger than FBGs and a LPG is typically about 30 mm long [32], compared to 5 mm for an FBG. Literature regarding LPGs has been published in a number of papers [23, 24, 48-50]. In the literature the work by Vengsarkar *et al.* [49, 51] is typically referred as the primary source that demonstrates the coupling from the fundamental guided mode, in a single-mode fibre, to forward-propagating cladding modes, utilizing LPGs with UV writing. However, before their work, several studies of related functionality were reported e.g. blazed grating in a two-mode fibre to induce $LP_{01} \leftrightarrow LP_{11}$ mode conversion [52], and in fact the basic ideas were originally demonstrated in microwave engineering many years previous [53].

LPGs couple light from the fundamental-core-mode in a single-mode optical fibre into modes confined to the cladding (cladding-modes), if there is sufficient modal overlap between a core and cladding-mode in the waveguide. Figure 5 illustrates the electrical field distribution before and after a LPG.

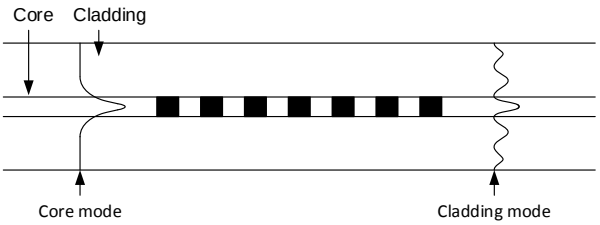


Figure 5 – Illustration of field distribution before and after a LPG, from [18]

The cladding-modes propagate in the same direction as the fundamental core-mode, opposite to FBGs where the light is reflected at the grating. The cladding is a very poor waveguide and coupled light is subsequently lost through absorption and scattering losses. This is apparent as loss in the transmission spectrum. For an embedded sensor in a wind turbine blade, it is required that the optical fibre is returned to the rotor Hub, for interrogation of the transmitted signal [18]. This is a fundamental difference to the typical method of interrogating FBGs where the reflected spectrum is measured and therefore the measurement is single ended.

A part of the cladding-mode field penetrates through the external boundary, and cladding modes are therefore sensitive to the surrounding of the optical fibre e.g. the RI. This is different withFBGs where the light primarily propogates in the core and is protected by the cladding. The RI of the coating is typically higher than the RI of the cladding (cladding-mode stripping coating). Therefore there is only partial reflection at the cladding-coating boundary. For cladding-modes to persist, it is needed to have an RI-change, preferably a drop, at the cladding-to-coating boundary to ensure total reflection i.e. the RI of the coating is lower than the RI of the cladding. For cladding modes with an incidence angle at the cladding-coating boundary, which is below the critical angle, the cladding-mode power will slowly diminish due to the radiation leakage into the polymer coating, where the radiation is soon absorbed or scattered [54], so the imaginary part of the propagation-constant in the coating material cannot be ignored compared to the real part and the coupling strength of the LPG [18].

The discrete wavelength at which coupling occurs is given by the phase-matching condition [55]:

$$\lambda^{(m)} = \left[ n_{eff} - n_{cl}^{(m)} \right] \Lambda \tag{4}$$

Where $n_{eff}$ is the effective index of the guided mode, $n_{cl}^{(m)}$ is the effective RI of an azimuthally symmetric cladding mode of order $m$ (for unblazed gratings), and $\Lambda$ is the spatial grating period. (The asymmetric modes can also to some smaller degree be excited).

LPGs can be produced by several methods such as mechanical pressure from plates [56], acoustically induced micro-bending [57] and splice-based controlled arc [58]. However, UV-illumination [51] through an amplitude mask is typical the preferred method. Due to the larger period, LPGs have the advantages that the demand for accuracy in production of LPGs is less critical, compared to FBGs production, hence a phase mask is not required. Figure 6 shows a measurement of the transmission spectrum for a typical commercially available LPG, with a centre wavelength of 1532 nm and a FWHM of 19 nm.

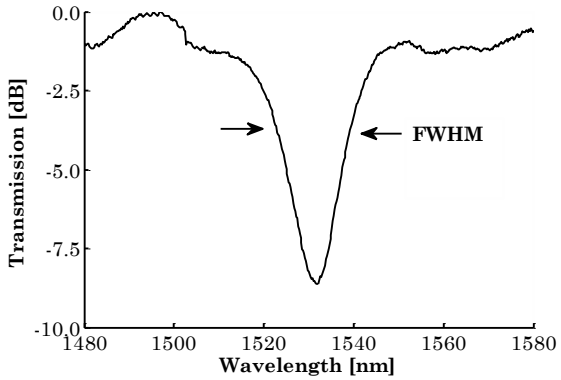


Figure 6 – Normalized transmission spectrum from a LPG, from [18]

The FWHM for LPGs is larger compared to FBGs, 20 nm vs. 0.2 nm, limiting the number of cascaded gratings in one fibre sensor compared to the number for FBGs. Since the resonance-wavelength depends on the difference between the core and cladding index, LPGs are more wavelength-sensitive to decay of grating strength [59]. Accelerated aging experiments have demonstrated that over a predicted lifetime of 25 years, the centre wavelength can change < 0.02 nm at 313

K (40 °C) and < 0.12 nm at 333 K (60 °C) [59]. This must be taken into consideration in the design for a given application and the expected working temperature of the application.

**Temperature Sensitivity**

LPGs are sensitive to temperature and strain due to changes in the fundamental- and the cladding-modes effective refractive indices and the change in grating period. Using the chain rule of derivatives, the sensitivity to temperature can be obtained from Eq. (4) as [55]:

$$\frac{d\lambda}{dT} = \frac{d\lambda}{d\left(\delta n_{eff}\right)}\left(\frac{dn_{eff}}{dT} - \frac{dn_{cl}}{dT}\right) + \Lambda\frac{d\lambda}{d\Lambda}\frac{1}{L}\frac{dL}{dT} \tag{5}$$

Where $\lambda$ is the centre wavelength of the attenuation band, $T$ is the temperature, $n_{eff}$ is the effective RI of the fundamental mode, $n_{cl}$ is the effective RI of the cladding mode, $\delta n_{eff} = (n_{eff}\text{-}n_{cl})$, $L$ is the length of the LPG and $\Lambda$ is the period of the LPG. The first term on the right-hand side is the material contribution, and is related to the change in the differential RI of the core and cladding from the thermo-optic effects. The second term is the waveguide-contribution as it results from changes in the period. With an appropriate selection of fibre-composition and grating-period it is possible to balance the two contributions and suppress temperature drift for a LPG sensor. For unbalanced LPGs in optical fibres, the typical temperature sensitivity is in the range of 5-15 nm/100 K [60], however, it depends on the fibre composition and grating period [18]. The centre wavelength depends on the RI of the coating material. Therefore it is possible to optimize the coating material for temperature compensation. LPGs in typical germanium-doped silica core fibre have a shift $(d\lambda/dT)$ towards longer wavelengths, due to positive $d(n_{eff}\text{-}n_{cl})/dT$. Selecting a coating material where the RI increase with temperature can provide suppression of temperature drift. However, conventional polymer for recoating has normally a negative $dn/dT$. With boron co-doping it is possible to design the optical fibre to have a $(d\lambda/dT)$ shift towards shorter wavelengths and thereby suppress temperature drift. Others have demonstrated a suppression of about a factor of 100, with shift as low as 0.07 nm/100 K [60].

**Strain Sensitivity**

LPGs are also sensitive to axial strain and it is given by [55]:

$$\frac{d\lambda}{d\varepsilon} = \frac{d\lambda}{d\left(\delta n_{eff}\right)}\left(\frac{dn_{eff}}{d\varepsilon} - \frac{dn_{cl}}{d\varepsilon}\right) + \Lambda\frac{d\lambda}{d\Lambda} \tag{6}$$

The first and second terms on the right hand side are termed material and waveguide contributions. The material contribution results from the strain optics (change in RI) and Poisson's effect, while the waveguide contribution depends on the slope $d\lambda/d\Lambda$ of the characteristic curve of the resonance band. Typically for a LPG with $\Lambda > 100\ \mu m$, the material contribution is negative, while the waveguide contribution is positive. For $\Lambda < 100\ \mu m$ both contributions to the strain sensitivity are negative [32, 55]. Thereby the sensitivity can be tuned by the selecting the period and fibre composition, creating either an enhanced sensitivity or an insensitive sensor. Bhatia *et al.* have for example demonstrated strain sensitivity for LPGs of 0.04 pm/με and -2.2 pm/με with different grating periods [55]. The typical strain sensitivity for a LPG in a SMF-28 fibre is ~1.5 pm/με [61].

LPGs can measure strain and temperature with an optical spectral sensitivity almost an order-of-magnitude higher than FBGs [49], giving the possibility of utilizing it as strain or temperature sensor [62]. However the effective resolution is limited due to the large FWHM for a typical LPG.

**Bend Sensors**

LPGs have the potential as a bend sensor. A bend direction asymmetry has been demonstrated for the resonance wavelength shift in one direction [63, 64]. It is possible therefore by combining a minimum of two LPGs to create a directional bend sensor [65].

When a LPG is being bent, new dips in the spectrum can appear [66, 67]. The new dip in the transmission band is normally significantly weaker and is typically in the range of 10 nm shifted from the original dip. The wavelength separation, between the fundamental dip and the second dip, increases with increased curvature of the bend [67]. The splitting depends on the effective RI difference of the two cladding modes, and not on the difference between the RI of the core and cladding mode. Therefore the splitting will not be affected by (to first order) cross-sensitivity to temperature, strain and RI changes [68]. Under temperature drift, the wavelength-distance between the two dips will not change (to first order), only the absolute wavelength of both dips will change [69]. Therefore the absolute wavelength shift can be interrogated for bend/curvature measurements and the splitting can be utilized for temperature compensating. Figure 7 illustrates the principle of splitting in the transmission spectra when a LPG is being bent. Dip 1 is the original transmission dip and dip 2 is the new dip.

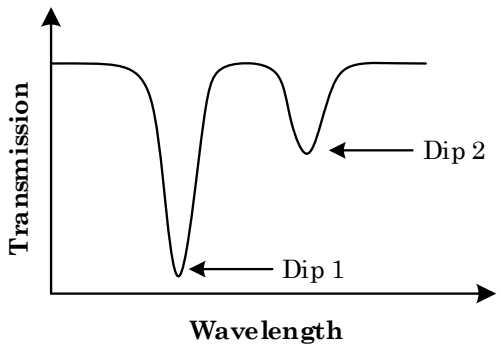


Figure 7 – Illustration of splitting of a LPG resonance, from [18]

In the literature the splitting has in several papers [69-71] been explained by stating that the fibre-curvature breaks the degeneracy of the cladding modes that are normally coupled to in the straight fibre. These non-degenerate modes, with power concentrated on opposite sides of the fibre core, then propagate with different speeds due to the difference in longitudinal strain above and below the fibre axis.

However, with numerical modelling, Block *et al.* [72] analysed modes of a curved three-layer optical fibre. They found that the splitting is caused by asymmetric changes of the effective indexes of the cladding modes and the core mode, which breaks the cladding-mode symmetry. This explains why the original attenuation dip, present in the straight fibre, shift in wavelength as curvature is increased. Allowing coupling to cladding-modes with higher order azimuthal symmetry than allowed in a straight fibre, which results in new dips at nearby wavelengths. Furthermore it has been experientially demonstrated that the strengths and the positions show no significant polarization dependence [58].

**Directional Bend Sensor**

The splitting can occur in a straight fibre (like an offset) if the geometry of the fibre is designed such that the core is not symmetrically in the centre of the fibre [68, 73]. This was demonstrated by Rathje *et al.* in 1999 with an optical fibre having a Core Concentricity Error (CCE) of 2.4 μm. This provides a direction-sensitive fibre-optical bend sensor based on LPGs [68, 73]. To increase the sensitivity the asymmetry can be increased, simply by a larger CCE [74]. However the CCE must be designed for a given application to optimize the sensitivity to bend, but without limiting the dynamic range.

The changes in splitting and the amplitude of the curvature are approximately linear, but with curvature around 0 $m^{-1}$ (straight fibre) the sensitivity has been observed to be lower [75]. This needs to be taken into consideration in the design of a given sensor, for example by a small pre-bend of an embedded fibre if the sensitivity in the region of 0 $m^{-1}$ is critical. The direction the fibre is sensitivity to can be determined by the CCE with light diffraction [75, 76]. However this process requires high precision and is therefore time consuming and a costly process when embedding a sensor. Furthermore typical methods for production of optical fibres

are optimized to avoid CCE (minimize CCE), therefore a fibre with a high precision of a specific CCE, is complex and costly.

Other asymmetrical fibres where the core is not located in the centre of the cladding, such as D-shaped and multicore fibres, or fibres where the index profile is not symmetrical around the core, can also be useful for bend and direction sensing. This has for example been shown in a D-shaped fibre, in a four-core fibre and in flat-clad fibre [77-79]. Fibres where the cladding is flat on minimum on side, as D-shape fibres, is much more suitable for embedding as the flat-side can be aligned to a base-plate providing an easy alignment for a bend-direction sensitive sensor. Alignment to a base-plate also provides a suitable method/process for a sensor when embedded on a turbine, as the risk for error placing the sensors in the production-line is decreased. Furthermore, these fibres have been commercially available and utilized in other applications [77, 80, 81] and are more distributed than CCE fibres. D-shape fibres can also be fabricated with standard fibre production facilities.

**Discussion**

Sensors based on LPGs have not yet been implemented on wind turbine blades and are therefore not investigated as comprehensively as FBGs for this application. Research has been conducted on the utilization of fibre optical grating sensors for structural health monitoring on other structures such as aircrafts [82], bridges [83] and trains [84]. These structures are not subjected to as significant bending compared to a wind turbine blade and the work is therefore focused on strain measurement with FBGs, as the benefit of utilizing LPGs as bend sensors in these applications is negligible. On wind turbine blades the structural deformations are large enough to overcome the issues regarding the large spectral width of the LPGs, that otherwise is limiting the effective resolution of a LPG. However there are a number of uncertainties regarding the possibilities to utilize LPGs and in particular LPGs in special fibres such as D-shaped. Some of these include; the required resolution, embedding method and cascade-coupling of sensors in the same fibre are for example unknown. However, LPG sensors have been implemented in other structures, e.g. bonded to the surface of a steel plate using an unsaturated polyester adhesive [67] and embedded in capillaries

structures [85]. These examples indicate the possibilities open for embedding the sensors.

LPG sensors can offer another type of load sensors, than the typical ones based on FBGs, as they can be both directional and bend sensitive which is of interest for wind turbine blade sensing. However, as the LPG technology for load sensing on wind turbine blades is not matured, more research is required to clarify "show stoppers" especially regarding embedding, resolution and sensitivity. Hereunder the fibre design, such as correct geometry to be suitable for embedding and with required sensitivity and resolution. As LPGs differ from FBGs by having much longer period and having cladding-modes, that depends on the RI of the medium (coating) surrounding the optical fibre, the embedding is a critical aspect of research. Here the materials for embedding LPG sensors might be different from the materials used for FBG sensors. For example non-uniform strain in the adhesive, used for attaching the fibre to the wind turbine blade, might act differently on LPG sensors than on FBG sensors. Furthermore FBG and LPG decays different and the lifetime for and embedded sensor might be different.

Optimization of the sensor such as grating period, the order of the cladding-mode and fibre composition to suppress or increase temperature and/or strain sensitivity sufficiently can be part of the development phase. The number of cascade sensors in a fibre or in a number of fibres, lifetime is also typically placed in the development phase, as it requires extensive field tests to determine the minimum requirements and it depends on the specific design of a wind turbine blade such as length, material stiffness and physical design.

In summery extensive research and development is required to develop a LPG bend sensor into an alternative sensor system that is competitive with commercially available FBG sensor systems. Moreover the LPG bend sensor has the possibility to provide a new type of sensor that can measure the bend directly, which might be a more natural method of sensing the shape of and the load on the wind turbine blade. This may be exploited to give better performance of the wind turbine based on active optimization. In the following chapters in this thesis; the first phase of this research is presented. In particular the embedding of a sensor, the sensitivity/resolution and a test on a full scale wind turbine blade is demonstrated.

# 3. Sensor Fabrication

This chapter contains selection and design of a suitable optical fibre for this application. To provide a wind turbine blade load sensor, with a directional LPG based sensor, an asymmetrical fibre is required. First initial experiments on samples were performed. However for this project a suitable fibre was designed and manufactured.

## 3.1 Investigation on Fibre Samples

In the first phase of the project, the possibility for providing asymmetrical fibres from suppliers was investigated. KVH, USA, utilizes D-shape fibres in gyros, and others have demonstrated LPG in there D-Shape fibre [79], however they were not able to provide a fibre for this project. A quote from a large fibre manufacture was offered, but it was not satisfied for the needs in this application, mainly the specifications for the D-shape core-centre to flat-side distance was a too large. Some special fibre samples were provided from other suppliers, such as a 125 µm 4-core single mode fibre from Fibrecore ltd, England, figure 8, a SMF-28 D-shape from Fibretronix, Sweden, figure 9, and a 265 µm flat-clad fibre with a CCE of 3 µm, "ODO265", from The University of Sydney, iPL lab, figure 10.

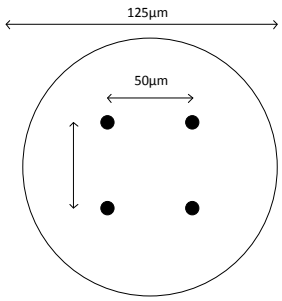


Figure 8 – Illustration of cross section of 4-core fibre

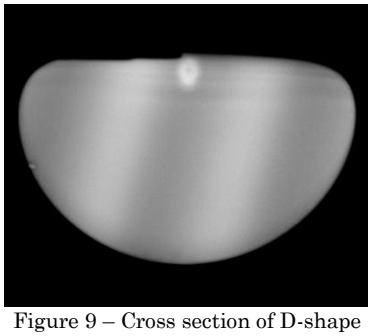

Figure 9 – Cross section of D-shape SMF-28

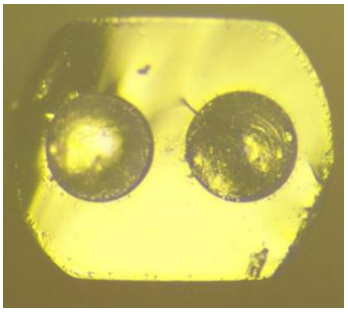

Figure 10 – Cross section of flat-clad fibre

The 4-core fibre is a photosensitive germanium and boron co-doped single-mode optical fibre. The distance between the cores is 50 µm and therefore it has an extreme asymmetry (CCE) for each individual core, making it interesting for a high sensitive sensor. A weak (few dB) LPG at 1550 nm was written into the fibre, with two dips (due to the asymmetry of the fibre), separated approximately 10 nm apart. Moreover the experiments revealed difficult alignment, e.g. an inferred camera at the end of the fibre to see the cores were needed for orientate the fibre correctly, and to avoid twisting. The difficult alignment process would be an issue when embedding into a wind turbine blade, therefore the fibre was not selected for this project.

After numerous attempts it has unfortunately not been possible to guide light above 1200 nm in the D-shaped SMF-28, not even in very short fibre lengths (15 cm). From the flat-side to the core-centre the distance is 5.3 µm, for a SMF-28, the typically Mode Field Radius (MFR) (at which the power density is reduced to $1/e^2$ of the maximum power density for a Gaussian approximation) is 5.4 µm at 1550 nm and this indicates that the fibre is very leaky, since the distance from the flat-side to the core-centre is shorter than the MFR. SMF-28 has a lower cut-off wavelength around 1250 nm, it might be possible that the loss for the single-mode is so high, only multi-mode light is transmitted. Note that the core is moved approximated 6.5 µm from the centre (closer to the flat-side), compared to a normal cylindrical fibre. Also note the "dent" on the flat-side, near the core, figure 9, this might influence the transmission. The work with the D-shape also revealed that the fibre have a small tendency to twist, which must be taken into consideration for embedding such fibre.

The "ODO265" has two flat-sides, CCE and large diameter, and is very interesting in an embedding process perspective, where the flat-sides is easy to align, robust against twisting, and very easy to handle with the large size. Twisting can be an issue with D-shaped fibres, this it is eliminated with two flat-sides. The fibre is a polarization-maintaining fibre due to the two large air holes. The fibre has CCE of 3 µm, which is a bit more than the 2.4 µm used by [68, 73], however this was in a typical 125 µm fibre, so directly compression is difficult. A relatively weak FBG was written in the fibre (a few dB), indicating a low photosensitivity. Despite a larger effort to align the fibre during writing, such as use of microscope camera to ensure non-twist and to have either the flat- or the round-side aligned perpendicular to the illumination angle, increasing to maximum illumination power and hydrogen loading, it has not been possible to write a single LPG in the

fibre. The two air circles can influence the writing process e.g. scattering of the UV-illumination. Furthermore the cladding-modes, which is possible to get confined, is influenced by the two circles. It might be that the dip is extreme broad (hundreds of nm), and therefore distinguish between a LPG and a saturated fibre is difficult. Despite the fibres good embedding potential, the inability to write a LPG on the fibre precluded the fibre from further research effort. Note all the above fibres were able to be spliced to standard SMF-28 fibre, with a manual controllable splicer, therefore only a small section of the special fibre can use for the sensor and standard fibre as transportation fibre, such that high loss in the special fibre is less critical.

## 3.2 Fibre Fabrication

### Design

Since it have not been possible to provide a suitable fibre from vendors or partners, collaboration with The University of New South Wales, Australia, for utilization of the recently commissioned joint national fibre facility to manufacture a suitable optical fibre, was established. This provides a large flexibility for the required fibre, since direct involvement in the process was possible during stays abroad. Based on the knowledge gained with fibre samples and the possible manufacturing process, a D-shape design of the fibre was selected.

The specifications for the manufacturing of a preform and fibre at UNSW was based on standard photosensitive fibre and results from [78] where they used a D-shaped fibre with a distance from the core-centre to the flat-side of 9 μm. They obtained sensitivity to curvature of $12.55 \cdot 10^{-9}$ m$^2$ (others using larger distance (16 μm) have only demonstrated ~$2.5 \cdot 10^{-9}$ m$^2$ [79]). The maximum curvature for a modern wind turbine blade is in the range of 0.01 m$^{-1}$. This gives a maximum wavelength change of 125.5 pm:

$$12.55 \frac{nm}{m^{-1}} \cdot 0.01 m^{-1} = 125.5 pm \tag{7}$$

Vestas asked for a resolution in the range of about 1% of the maximum curvature, which corresponds to resolution of 1.25 pm, typically about the limited for commercial interrogators for FBGs.

The sensitivity is partly given from the asymmetry and from the fibre composition, the aim was a D-Shape fibre with a distance from the core-centre to flat-side slightly shorter than the 9 µm to provide better sensitivity, however recall from chapter 3.1 a too small distance (5.4 µm) might give a fibre with very high loss. A distance of 7-8 µm from the flat-side to the core-centre was therefore selected. Table 1 is a list of the selected specifications. The fibre radius, Mode Field Diameter (MFD), dispersion and coating is selected based on a typical SMF-28 fibre. Standard germanium doping for photosensitive fibre was selected. The cut-off was selected so the fibre was suitable for use in the 1500 nm low-loss window.

| Fibre specifications | |
|---|---|
| Fibre radius | (r) = 62.5 µm +/-1 µm |
| Distance from core-centre for flat-side | x = 7-8 µm |
| Mode field diameter | 9.5 +/-0.5 µm |
| Cut off λ | 1200-1500 nm |
| Zero dispersion λ | 1310 nm |
| Dispersion at 1550 nm | 17 ps/nm/km |
| Doping | Germanium |
| Coating diameter | 250 +/-10 µm |

Table 1 – Design parameters for D-shape fibre

**Preform Manufacturing**

The preform manufactured at UNSW, employs the Modified Chemical Vapor Deposition (MCVD) process on a lathe similar to the illustration in figure 11. The MCVD process technique was first reported in 1974 by MacChesney *et al.* [86] and is widely used for fibre optical preform manufacturing, due to relatively easy

implementation [87]. The MCVD process is based on the high temperature oxidation of reagents inside a rotating tube which is heated by an external source.

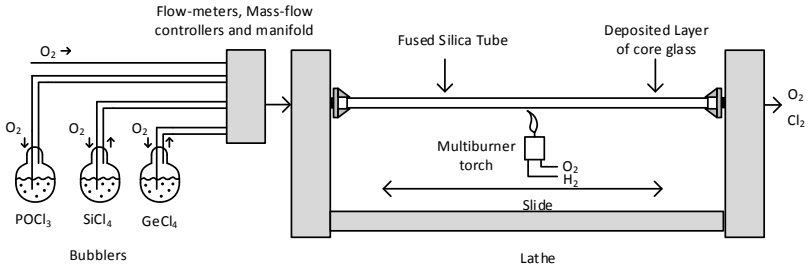


Figure 11 – Illustration of preform lathe

First a standard Heraeus silica tube was setup on the lathe, heated-up with a multi-burner over the tube length and then Phosphoryl chloride ($POCl_3$) was used for cleaning the tube, with $O_2$ utilized as carrier. At 1800°C the inner cladding was built up with silicate ($SiO_2$) during 15 passes during preform depositions before a core layer of germanate ($GeO_2$), phosphorus pentoxide ($P_2O_5$) and silicate was deposited over one pass, given a germanate doping of 4.5 mol. % and 1.0 mol. % of $P_2O_5$ (for photosensitivity and to increase the RI of the core [88]). The tube was then collapsed at 2200°C, see figure 12. This was the first successful preform manufactured at the new joint fibre facility.

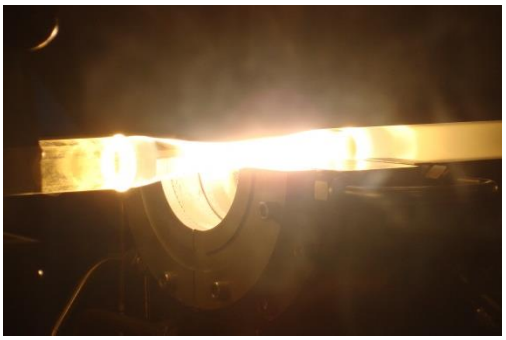

Figure 12 – Collapsing the preform tube

The index profile of the manufactured preform was measured using a Photon Kinetics 2600 Preform analyser at UNSW. The Preform analyser utilizes a laser at 633 nm and oil with a RI of 1.46. To estimate the RI at 1550 nm the "Sellmeier formula", with values for fused silica, has been used [89]:

$$n(\lambda)=\sqrt{1+\frac{0.6961663\lambda^2}{\lambda^2-(0.0684043)^2}+\frac{0.4079426\lambda^2}{\lambda^2-(0.1162414)^2}+\frac{0.8974794\lambda^2}{\lambda^2-(9.896161)^2}} \tag{8}$$

$\lambda$ is in micrometres. The difference between 633 nm and 1550 nm is found to be 0.0013, which is used to determine the core and cladding index for the preform at 1550 nm.

The normalized waveguide parameter $V$, determines the fraction of the optical power in a certain mode which is confined to the fibre core for a step-index fibre. For a single-mode fibre $0 < V < 2.4048$, the closer the $V$ value is to $2.4048$, the better the mode is confined, but the scattering losses in the core or at the core-cladding interface might increase. Above $2.4048$ the fibre is multimode, and at low $V$ values the fibre is sensitive to micro-bend losses and to absorption losses in the cladding. The calculation of the $V$ number is as follow [90]:

$$V=\frac{2\pi}{\lambda_0}a\sqrt{n_1^2-n_2^2} \tag{9}$$

The predicted core radius, $a$, is calculated by scaling down the preform diameter to 125 μm, giving a scaling value of about 106.3 (preform diameter: 13.3 mm).

The MFD, $\omega$, can be calculated from the following equation [90]:

$$\frac{\omega}{a}\approx 0.65+\frac{1.619}{V^{3/2}}+\frac{2.879}{V^6} \tag{10}$$

The data for the preform is presented in table 2, where *position* is the distance from one selected end of the preform, see figure 13. *OD* is the diameter of the preform, *Core OD* is the diameter of the core the preform, *Core RI* is the RI of the core, *Clad RI* is the RI of the cladding, *Δn* is the difference in RI of the core and cladding. It is seen that from 106 mm to 309 mm the preform provides suitable values.

| Preform Measurements | | | | | | | | |
|---|---|---|---|---|---|---|---|---|
| Position | OD | Core OD | Core RI | Clad RI | Δn | MFD | V | a |
| 106 mm | 13.29 mm | 0.71 mm | 1.45271 | 1.44815 | 0.0046 | 11.30 µm | 1.547 | 3.32 µm |
| 149 mm | 13.23 mm | 0.68 mm | 1.45270 | 1.44810 | 0.0046 | 11.42 µm | 1.503 | 3.21 µm |
| 229 mm | 13.31 mm | 0.66 mm | 1.45228 | 1.44795 | 0.0043 | 12.34 µm | 1.407 | 3.10 µm |
| 309 mm | 13.23 mm | 0.64 mm | 1.45185 | 1.44784 | 0.0040 | 13.66 µm | 1.321 | 3.02 µm |
| 389 mm | 13.23 mm | 0.64 mm | 1.45150 | 1.44784 | 0.0037 | 15.15 µm | 1.262 | 3.02 µm |
| 469 mm | 13.29 mm | 0.63 mm | 1.45090 | 1.44784 | 0.0031 | 20.01 µm | 1.131 | 2.96 µm |
| 549 mm | 11.00 mm | 0.52 mm | 1.44930 | 1.44778 | 0.0015 | 85.09 µm | 0.794 | 2.95 µm |

Table 2 – Parameters for the preform

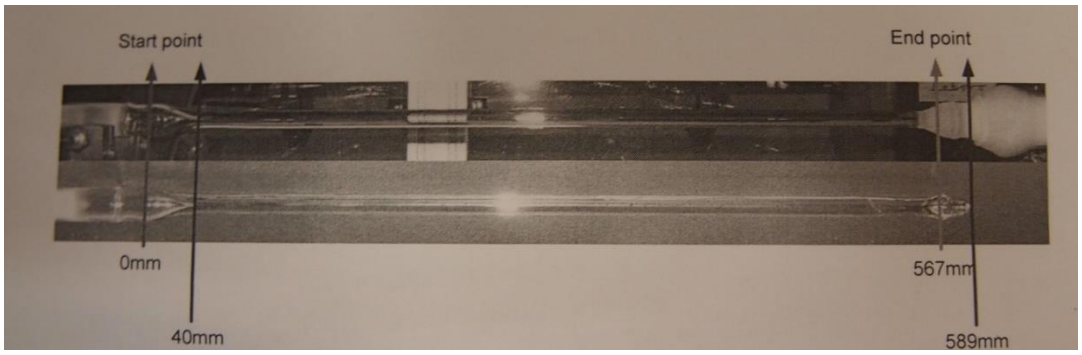


Figure 13 – Positions at the preform

Figure 14 shows the index profile at the first section (106 mm). Note the raised inner cladding which is due to the cladding deposition. The step between the inner and outer claddings is mainly because of the material composition difference: inner – doped cladding; outer – silica tube. The size of the inner cladding is approximately 3 mm, given a 200 µm deposit at each pass. The dip in the core, is

typically, and due to germanate loss (diffusion/evaporation) during the preform collapse, and is typically smoothened during drawing (diffusion through homogeneous material).

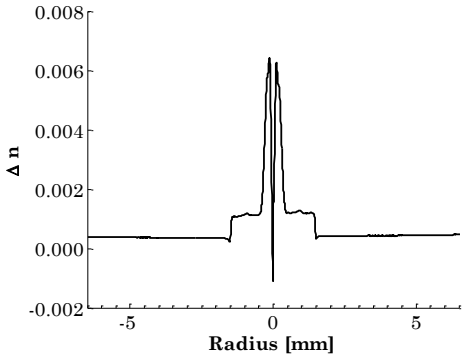


Figure 14 – Index profile at position 107 mm of the preform, from [91]

The preform was divided into a number of 6 sections *PA* to *PF*. The first section *PA* 70 – 140 mm and second section *PB* 140 – 210 mm were milled into a D-shape preform using a LECO VC-50 cutting machine. Preform *PA* was milled down such that when drawn down to a 125 µm fibre the distance from the core-centre to the flat-side would approximately be 7 µm, illustrated in figure 15. *PB* was milled down such that the distance for a 125 µm fibre would be 9 µm. When drawn, the fibre diameter can be slightly change and thereby changing the core-centre to flat-side, providing a number of different distances.

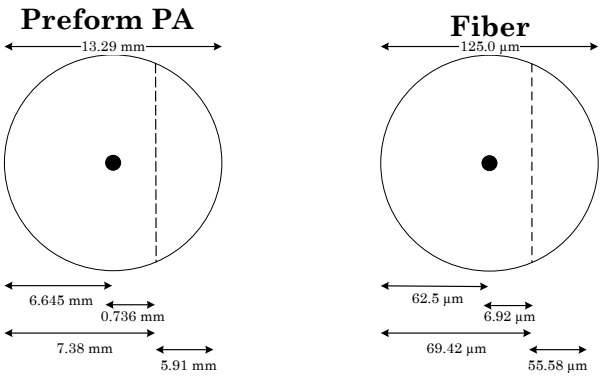


Figure 15 – Preform *PA* scaling down to fibre dimensions

Figure 16 shows the *PA* after milled down to a D-shape, the preform is colour marked for knowing the positions, and the marks was removed and cleaned properly before drawing. A preform of 70 mm would provide a few hundred meters of suitable fibre when drawn, which is more than enough for this project.

Figure 16 – PA preform milled down to a D-shape

**Fibre Drawing**

The preforms were then fused together with a lead, a piece of extra silica for the drawing start and a base to attach the preform to the feed in the draw tower. The preforms were flame polished to remove dirt and even the flat-surface from marks from the cutter. The preform was then drawn in stages on a customised draw tower, illustrated in figure 17. To balance outer diameters, core-centre to flat-side distances and D-shape, the drawings was performed at a low temperature of 1860 °C and at an appropriate speed of 18 m/min. For comparison, the speed for a normal circular preform, with parameters similar to D-shaped preform, would be drawn at 40 m/min and 1920 °C at this fibre drawing setup. The temperature and speed were slightly changed at different sections of the preform, to change the geometry (diameter), and thereby providing a various number of core-centre to flat-side distances.

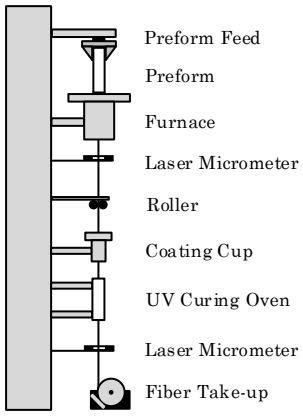


Figure 17 – Illustration of draw tower

The different fibre sections were characterised under a microscope, to determine their individual sizes. A cross-section of the best suitable section, from *PA*, is shown in figure 18, note the inner-cladding with has a radius from the core-centre of about 35 µm. Also note the bulge on the flat-side near the core, which is due to different material expansion. For this research project the shape is acceptable. However in a development process, for a commercial sensor, this can be further optimized with a different fibre composition, to minimize the bulge. The fibre diameter was measured to be 156 µm and table 3 shows the fibre parameters, calculated for this diameter.

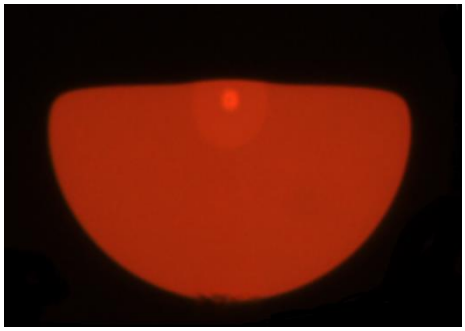

Figure 18 – Picture of the cross-section of the D-shape fibre, from [91]

| Fibre parameters | | | | | |
|---|---|---|---|---|---|
| OD | Core OD | V | MFR | Core – flat-side | Cut-off |
| 156 µm | 8.3 µm | 1931 | 5.4 µm | 7.5 µm | 1245 nm |

Table 3 – Parameters of fibre from preform PA

With a diameter of 156 µm the core-centre to flat-side is 7.45 µm, which are in the middle of the specifications. The MFD is a bit larger than specified, however the important distance from the MFR to the flat-side is about 2 µm, given a larger distance than the sample of the D-shaped SMF-28.

The fibre was tested regarding transmission loss, with a 1550 nm broadband-source launched into a SMF-28 fibre and with a measured output power of 3.9 mW. The SMF-28 was end-fire coupled to the D-shape fibre. With the standard coating the power after the 1m D-shape fibre was 750 pW. The coating was chemical removed, and the transmitted power was measured to 1.1 mW. The fibre was cleaved at 0.5 m and the power was measured to 1.5 mW. This gives a fibre loss of ~2.7 dB/m. The end-fire coupling loss is ~3 dB.

**Discussion**

This was the first preform and first non-circular fibre fabricated at the new facility, and overall it was very successful. A number of D-shape fibres, about 400 m in total, with different sizes was drawn. The core was Germanium doped with 4.5 mol. %, which is rather low for a photosensitivity fibre, however as the expansion coefficient for germinate and silicate are different, a low doping is need to retain the D-shape during drawing, and even with this low doping there is a bulge on the flat-side of the fiber. The MFR is not perfectly aligned to SMF-28, therefore Fresnel reflections can occur when coupling between the fibers. A suitable fibre was selected for future work, the diameter is 156 µm and the core-centre to flat-side is 7.45 µm, the important distance from the MFR to the flat-side is about 2 µm. Recall from chapter 3.1 a distance similar to the MFR might give very high loss. But a small distance is stated for optimized sensitivity to bend. Therefore this distance is a good trade-off. The loss in the fibre about 2.7 dB/m, a rather high loss (fibre length out and return in a blade is about 100 m), however it would be spliced to standard telecommunications fibre and approximately only 0.5 m of the D-shape would be used for each sensor and therefore it would not be an issue regarding signal power for light source/interrogator. The coupling loss with end-fire coupling was also rather high (matching index gel not possible due to D-shape), however splicing would provide better results and in a final application the fibre parameter can be further optimized to match standard fibres for better coupling.

The D-shape fibres have been subject for experiments regarding self-assembly of silica-nanoparticle layers on the flat-side (surface) of the D-shape. This work has been published as [92-94].

## 3.3 Grating Fabrication

### Ramsey Fringes

As mentioned in chapter 2 the bandwidth (FWHM) of a LPG resonance is very broad, which results in limited effective resolution for interrogating their resonant dip and shift. Moreover, it is possible optimize with the general principle of interaction between a particle and two consecutive oscillatory fields, developed originally by Ramsey [95]. Here LPGs in an optical fiber act as a Mach-Zehnder (MZ) device in transmission [96], illustrated in figure 19. The first LPG couples a proportion of the propagating core-mode into the cladding-mode. The two modes propagate independently until they reach the second LPG, at which the power in the core- and cladding-modes constructively interferes and propagates in the output core-mode [97]. This provides narrow resonances fringes for high-resolution detection of the sensing parameter and reduced sensitivity to noise [95]. The fringes separation is proportional with the effective separation between the two LPGs. For maximum interference visibility, in the lossless case, each of the LPGs should ideally be 3 dB deep [95], such that the power is equally split into the two modes allowing interferences with 100% visibility. This principle has been demonstrated for various applications such as RI sensors [98, 99], as highly sensitive sensor for cure monitoring of UV-epoxy resin [100] and also for bend sensing in symmetrical fibers [101].

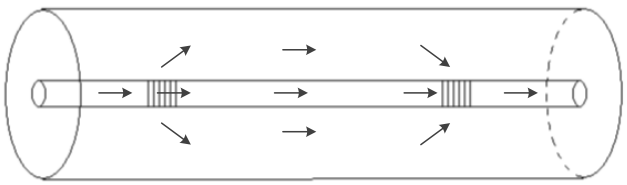

Figure 19 – Illustration of LPG Mach Zhender in an optical fibre

**Modelling – Fringes Spacing**

The transmission spectra from a LPG can be calculated by the piecewise-uniform approach based on 2x2 matrices, where the grating is divided in $M$ uniform sections of the grating, typically *M~10-1000*, [24, 96, 102]. $F_i$ is the fundamental mode amplitude and $S_i$ is a different mode traveling in same direction. For LPGs the start is $F_0=F(-L/2)=1$ and $S_0=S(-L/2)=0$, $L$ is the length of the grating, and calculated to $F(L/2)=F_M$ and $S(L/2)=S_M$. $P_{in}$ is input power of the fundamental mode. Figure 20 illustrates the definitions for transmission gratings.

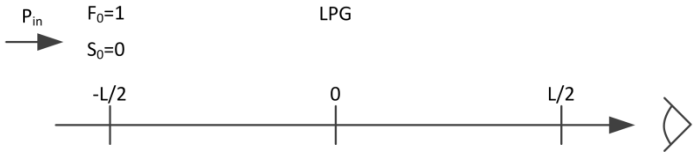


Figure 20 – Illustration of definitions of $F_0$ and $S_0$, from [18]

For LPGs the matrix of each section is given by [24, 96, 102]:

$$T_M = \begin{bmatrix} \cos(\gamma_C \Delta z) + i\frac{\hat{\sigma}}{\gamma_C}\sin(\gamma_C dz) & i\frac{\kappa}{\gamma_C}\sin(\gamma_C \Delta z) \\ i\frac{\kappa}{\gamma_C}\sin(\gamma_C \Delta z) & \cos(\gamma_C \Delta z) - i\frac{\hat{\sigma}}{\gamma_C}\sin(\gamma_C \Delta z) \end{bmatrix} \quad (11)$$

For a uniform grating, $\gamma_C \equiv \sqrt{\kappa^2 + \hat{\sigma}^2}$, $\hat{\sigma}$ is a "DC" self-coupling (period-averaged) coupling coefficient, $\kappa$ is an "AC" cross-coupling coefficient and $\Delta z$ is the length of grating.

Once all matrices for the individual sections are known, the output amplitudes can be calculated as:

$$\begin{bmatrix} F_M \\ S_M \end{bmatrix} = T \begin{bmatrix} F_0 \\ S_0 \end{bmatrix}; \quad \mathrm{T} = T_M \cdot T_{M-1} \cdot \ldots \cdot T_i \cdot \ldots \cdot T_1 \quad (12)$$

The transmission spectrum of a composite grating, as in a MZ configuration, can be found with the following procedure [103]:

$$\begin{bmatrix} F \\ S \end{bmatrix} = T_2 \cdot T_P \cdot T_1 \begin{bmatrix} 1 \\ 0 \end{bmatrix} \tag{13}$$

The amplitudes of the incident core- and cladding-modes are here normalized (1 and 0). $F$ and $S$ are the complex amplitudes of the core- and cladding-mode. $T_2$ and $T_1$ are in this case identical gratings. In the MZ case $T_P$ is the phase shift from the distance between the gratings and is given by [96, 103]:

$$T_P = \begin{bmatrix} \exp\left(i\frac{\Delta\varphi}{2}\right) & 0 \\ 0 & \exp\left(-i\frac{\Delta\varphi}{2}\right) \end{bmatrix} \tag{14}$$

Where $\Delta\varphi = 2\pi\Delta nL/\lambda$, $L$ is the length between the gratings.

Figure 21, illustrates a simulation of a LPG pair acting as a MZ interferometer. The dashed line is the first ~3 dB LPG and the solid line is the output of the MZ interferometer. The grating period is $\Lambda$ = 430 μm, grating length 1 cm, $\Delta n_{eff}$ = *0.0036* in the grating, $\Delta n_{eff}$ = *0.0035* between the gratings, 10 cm separation from end of gratings. Note the centre dip is very deep ~50 dB and narrow FWHM ~3 nm, compared to a typical LPG of 20 dB and 20 nm FWHM, increasing the effective resolution. Due do imperfection and loss such strong fringes is difficult to implement in practice.

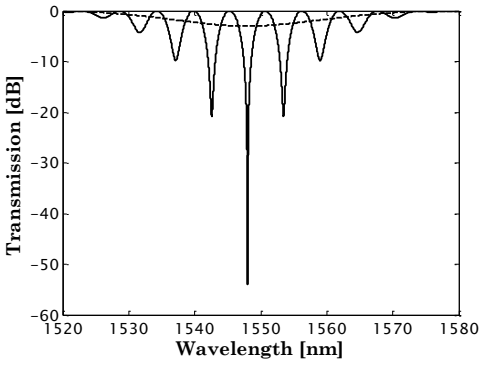


Figure 21 – Normalized spectra of MZ simulation

Note that loss is not included in these simulations, the loss has most influence for small side-lopes and for strong gratings, furthermore the gratings are assumed uniform, however in practise a UV-written LPG would always have some minor apodization due to the beam profile of the UV laser. Furthermore Fresnel reflections from splices and from the UV index change during writing are not included in the simulation, but would have a minor influence on a grating in practice. The coupling coefficients are assumed to be 1 (as the transverse distribution of a UV-induced changes are unknown), this might affect $\gamma_C$ in the calculation.

**Grating Writing**

Together with partners at iPL, The University of Sydney, collaboration for writing of gratings was established. The laboratory facilities have different setups for UV-writing, for this project a 193 nm Excimer Laser (ArF) was utilized mainly as it provides the highest power of the setups. To avoid cracks on the surface during coating stripping, and thereby retain the strength of the fiber, all coating stripping was utilized with chemicals. When writing LPGs, approximately 50 cm of D-shape were spliced to standard SMF-28 fibers utilizing a manual controllable splicer, see figure 22. With the right parameters the D-shape is maintained (current and time), and the splice loss is minimized. The LPGs were inscribed without hydrogen loading. The D-shaped was aligned with the flat-side perpendicular to the illumination angle. Writing was done on a setup as illustrated in figure 23.

Figure 22 – D-shape fibre (left) spliced to standard SMF-28, from [104]

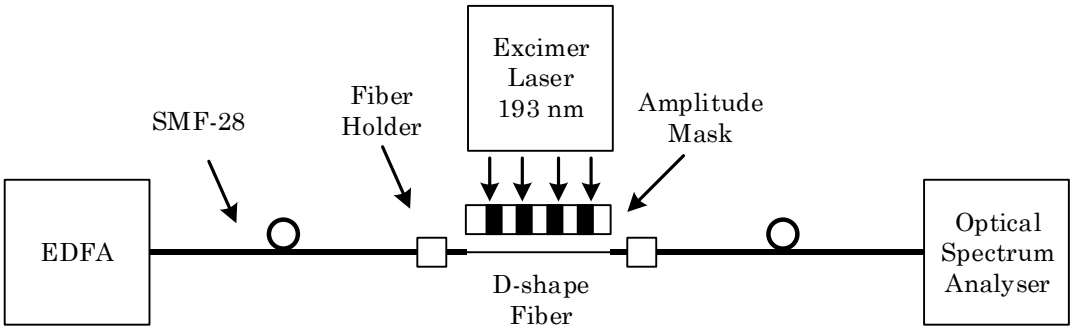


Figure 23 – Illustration of UV laser setup for grating writing

The UV laser energy was 385 mW, with a pulse repetition rate of 30 Hz and a writing time of about 15 minutes. The fundamental grating period for the 1550 nm range was found to be $\Lambda = 600$ μm (verified 300 μm was not fundamental), where a metal-mask with a 50:50 duty cycle was utilized. The written gratings were 40 mm long and separated 100 mm between the centers, as illustrated in figure 24.

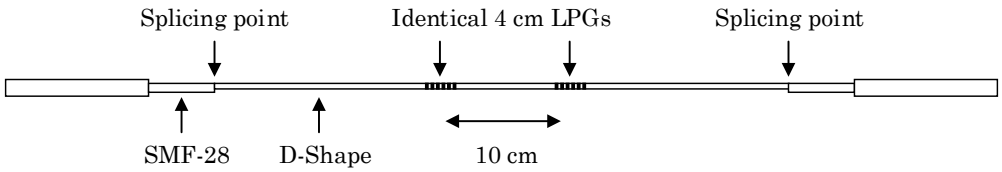


Figure 24 – Illustration of grating separation

The LPGs were observed in transmission with an erbium ASE source and an Optical Spectrum Analyser (OSA) using a resolution of 1 nm, during writing. The strength of the dips depends of the polarisation. Here an unpolarised ASE source was used, Fresnel reflections and coupling between SMF-28 and the D-shape give some polarisation mixing [20], and fine structure is observed (amplitude ripples). The LPGs are therefore written stronger than 3 dB so that they are clearly visible. These LPGs have approximately a ~10 dB transmission dip centre near 1560 nm. Two successful MZ sensors were written shown in figure 25, 26, 27 and 28*,

* Note, in [104] *sensor 2* was shown before embedding, this must have been *sensor 1*.

labelled *sensor 1* and *sensor 2* (dip of single LPG and MZ fringes respectively). Characteristic interference fringes associated with a MZ device in the transmission is observed, with good fringe contrast (~ 10 dB). A third sensor was written, however the dip appeared at 1509 nm, figure 29, indicating a slightly change in fibre parameters, the second LPG written in the fibre is misaligned and has a dip at 1530 nm shown in figure 30, this indicated the fibre is inhomogeneous (likely a change in the flat-side to core-centre distance) over the small 10 cm section. Figure 31 is a simulation of the separation of the fringes for a fibre with the same composition as the D-shape and the written gratings, with same assumptions as the simulation previous in this chapter. From equation (4), $\Delta n_{eff}$ is found to be 0.0026 for a dip at 1560 nm and with $\Lambda$ = 600 μm. The fringes separations in the simulation are shown to be 5.4 nm and the measured separations are about ~6 nm (dashed line first LPG, solid line MZ configuration). The difference between the simulation and the measurements is due to the assumption mentioned in chapter 3.3 "Modelling – Fringes spacing", however the calculated and measured separations is still in good agreement.

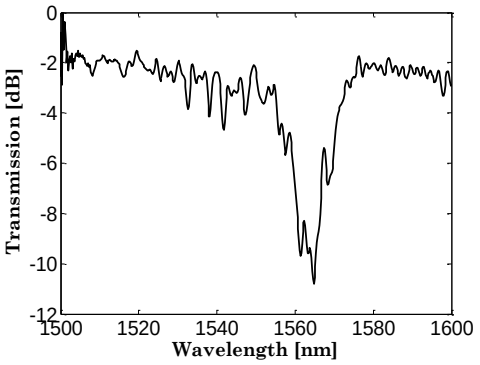


Figure 25 – Normalized spectrum of single LPG in D-shape fiber (Sensor 1), from [104]

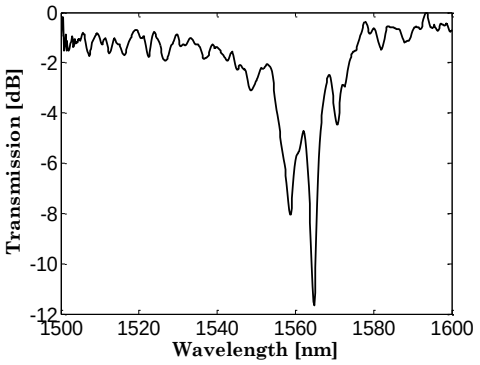


Figure 26 – Normalized spectrum of MZ fringes in D-shape fiber (Sensor 1), from [91, 104]

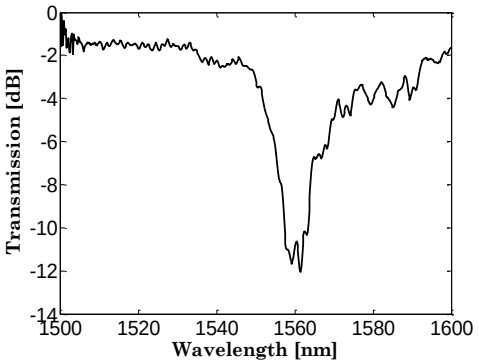


Figure 27 – Normalized spectrum of single LPG in D-shape fiber (Sensor 2), from [104]

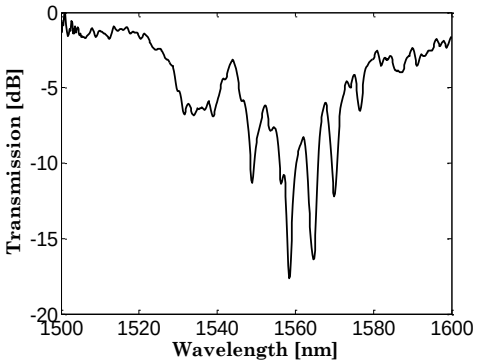


Figure 28 – Normalized spectrum of MZ fringes in D-shape fiber (Sensor 2), from [104]

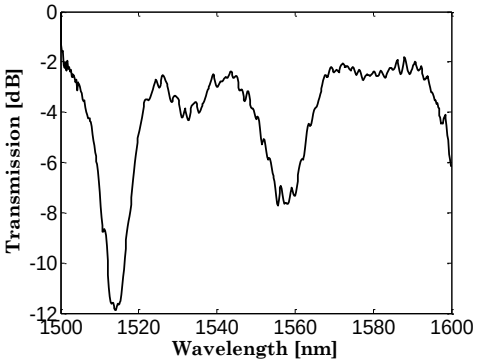


Figure 29 – Normalized spectrum of single LPG in D-shape fiber (Sensor 3)

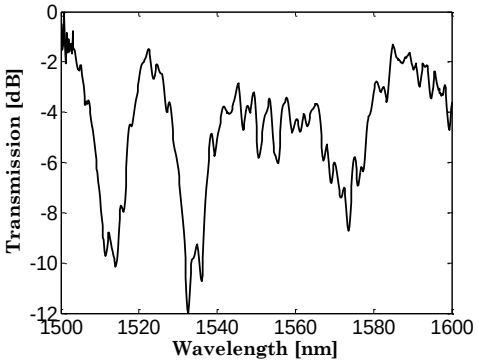


Figure 30 – Normalized spectrum of MZ fringes in D-shape fiber (Sensor 3), from [91]

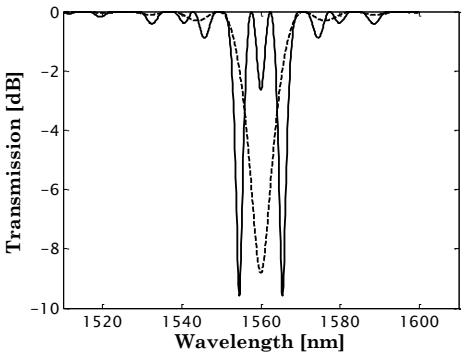


Figure 31 – Normalized spectra of the model of MZ configuration in D-shape fiber, from [91]

**Discussion**

Three sensors were produced, the resonance dip for *sensor 1* and *2* were both near 1560 nm and the dip for *sensor 3* was located near 1510 nm. All three had similar transmission depths (~10 dB). *Sensors 1* and *2* had MZ fringes, with *sensor1* showing two dips in agreement with the simulation, with a separation of ~6 nm similar to the separation in the simulation. The second sensor showed more fringes. The deepest dip in the spectrum and with the longer wavelength agreed well with the model. The shorter wavelength dips did not align well with the calculated fringe separations. This is subject to further investigation in the following chapter, where a model predicts the couplings between the modes. The second LPG resonance for the third sensor was misaligned and shifted about 20 nm towards longer wavelengths compared to the first LPG, indicating different fiber parameters for the gratings (surface distance). Furthermore the first LPG, in *sensor 3*, also shows a second dip near 1560 nm, this is also subject to future investigation in the following chapter.

The spectra have Fresnel reflections coming from the splices from standard fiber to the D-shape and coupling from a standard fiber to an asymmetrical fiber [20]. No reflections were seen in splicing and writing in the 4-core and ”ODO-265” flat-clad fiber, due to better matching to SMF-28 fiber. For a commercial sensor the D-shape fiber can be further optimized to match a SMF-28. The D-shape fiber was spliced to standard fiber with a manual controlled splicer, for a commercial sensor this can be performed automatically [105].

As the D-shape fiber is single mode from 1250 nm and the transport fiber have a relative short length (~100 m), the entire telecommunication band 1260 to 1675 nm (O- to U-Band) can be used. With an overall bandwidth of 20 nm as *sensor 1* an application with up to 20 sensors is possible.

# 4. Embedding, Characterisation and Testing Results

A reliable embedment method for sensors in wind turbine blade is critical [4]. An important aspect of this research project is the ability to embed LPGs directly into the matrix of the wind turbine blade. With this ability a very robust sensor can be provided, due to very good protection to the environment, especially for protection against water and salt for off-shore turbines. Wind turbines are located in various environments, and it is of significant importance that the spectral response of an embedded LPG does not change shape due to temperature changes and the embedment method. In this chapter, the embedment of a sensor into the adhesive utilized in the matrix of a wind turbine blade and the temperature response is investigated.

## 4.1 Embedding into Blade Material

**Recoating**

An optical fiber sensor is an ideal candidate technology for embedment into the matrix of a wind turbine blade due to material comparability [4]. A wind turbine blade consists typically of glass- and carbon-fibre (graphite) composite materials. These material typically have a Coefficient of Thermal Expansion (CTE) of ≈ $7 \cdot 1 \cdot 10^{-6}$ m/(m·K) and ≈ $2 \cdot 10^{-6}$ m/(m·K) respectively [106], however it is very dependent on the composition and the specific mixture and adhesive type, where the CTE for glass-fibre typically are higher than for carbon fibre and carbon fibre can be tuned in the resin matrix to have almost zero expansion. The CTE for a standard optical fibre is $0.55 \cdot 10^{-6}$ m/(m·K). All the CTE values are small expansions and the optical fibre CTE is similar to the one for carbon and glass-fibre, illustrating good material capability.

Initially in this work standard FBGs sensors were embedded into the adhesive, to provide knowledge of the influence on the spectral response, as earlier work with embedding of FBGs has indicated an issue when embedding them into other epoxy materials. The fibers were fixed with tape at both ends on a glass-fiber base-plate (before the adhesive was applied) to ensure the fibers were straight and with even strain before embedding. To ensure optimum quality the adhesive was applied

directly from the production line and cured with the standard production cure cycle. Figure 32 and 33 shows the spectra from a FBG without coating, before and after embedding respectively. Note typical suppression of side slopes is observed [95]. There is a negligible change in center wavelength and bandwidth and the quality of the response from the FBG is still sufficient for sensing.

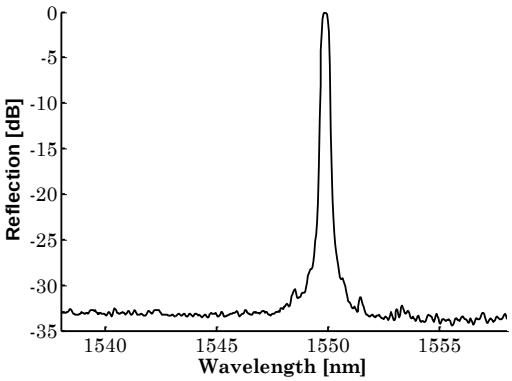


Figure 32 – Normalized spectrum from FBG before embedding

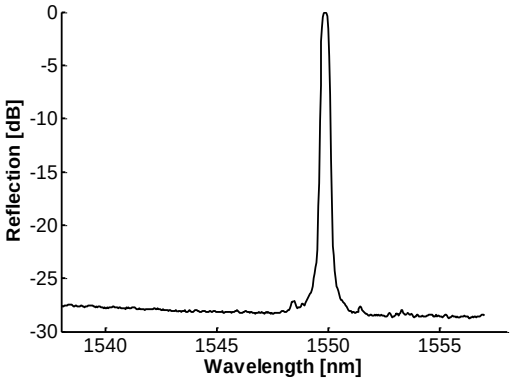


Figure 33 – Normalized spectrum from FBG after embedding

LPGs are sensitive to the RI of the surroundings (cladding-modes), and the property of the adhesive is more critical when embedding, compared to embedding of FGBs. A LPG in a standard fiber without coating was embedded with the same procedure as the FBGs. Figure 34 shows the spectra before and after embedding. The embedding results in a significant broadening and decrease of the depth of the dip, so the spectral response is no longer sufficiently deep and narrow for sensing. It is anticipated that the RI of the surrounding adhesive and micro-bending have a significant effect on the broadening of the spectra, therefore several methods were investigated for recoating a LPG, mainly methods suitable for a simple lab setups. As the LPG is sensitive to the RI of the soundings, focus was on a recoating material suitable to provide a low RI. For the cladding to coating interface a large index step is required as the transition has roughness (much more than a near perfect transition as the core to cladding transition), e.g. air bubbles. The RI of the investigated recoating material in this work is about 1.37 at 1550 nm, which is a about a factor 10 larger than the typical index change of $7 \cdot 10^{-3}$ for core to cladding transition and is more than sufficient.

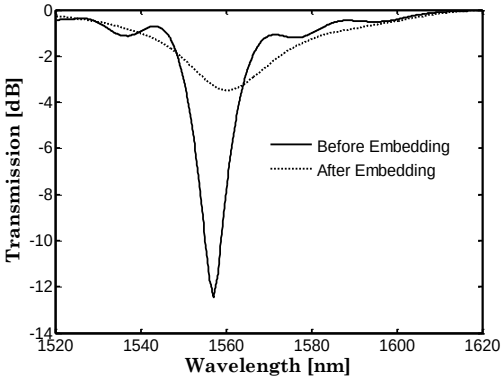


Figure 34 – Normalized spectra of a LPG before and after embedding in the adhesive, from [18]

Different low refractive recoating materials for optical fibers were investigated. Both temperature and moisture cured recoating material was applied with various techniques. However they all have the issue that the cured recoating was uneven as shown in figure 35. This gives changes to the spectrum such as a spectral shift, broadening and even splitting of the dip (micro-bend loss), an extreme case is shown in figure 37 where the spectrum has both split and decreased to a depth of 1.5 dB. The application method was refined; however it did not significantly improve the spectral performance of the sensor. Moreover, with a UV-cured recoating material a process providing suitable results was found. This recoating material is designed for use in commercial fiber drawing towers. The material must be applied in an inert atmosphere [107] ($N_2$ was utilized here) otherwise the recoating becomes tacky. The process for experiments here was similar to setups in draw towers; where a small setup (50 cm high) with a tube, cup, UV-box and a DC motor was build. Figure 36 shows a uniform recoated optical fiber (fiber painted red). Note for a large scale production, recoating machines are commercialized (relative expensive).

Figure 35 – Uneven recoated LPG

Figure 36 – Even recoated LPG (fiber painted red)

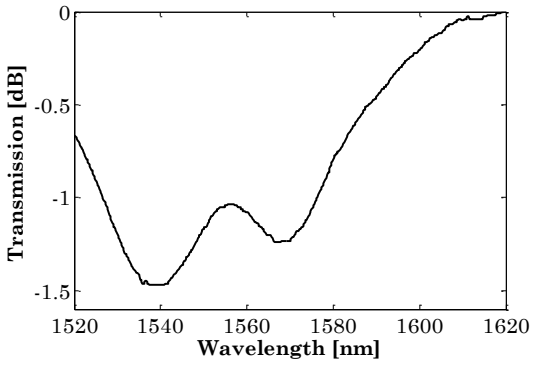


Figure 37 – Normalized spectrum of a bad recoated LPG

The recoated LPG was placed on a fiber-glass base-plate, and pre-fixed applying a small pre-strain (negligible wavelength shift), and embedded into the adhesive utilized in the matrix of a wind turbine blade [108]. Figure 38 shows the spectrum before and after embedding. The dip is suppressed from 8.8 dB to 7.6 dB, and the FWHM is increased from 8.7 nm to 11.0 nm, after embedding. The spectral response shows that there is no significant wavelength shift before and after embedding. However a small change of a few nm can occur [18] (strain and temperature affect this). The embedded LPG has a spectral response that is still distinct and suitable for sensing.

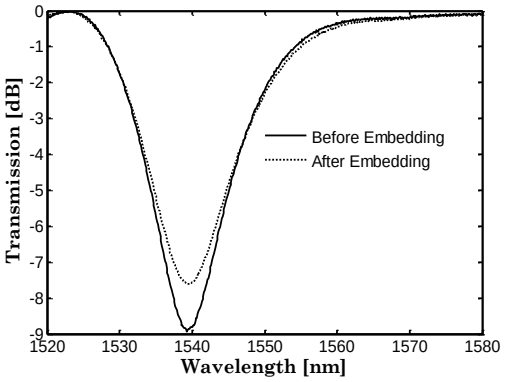


Figure 38 – Normalized spectra of an LPG before and after embedding, from [108]

**Strain and Temperature Response**

Strain/stress from the adhesive might influence the spectral response when embedding, especially under different temperatures. Therefore two FBGs were embedded with the adhesive together with a recoated LPG on a baseplate to investigate the influence from strain and temperature during the cure process and for temperature changes [108]. The setup is illustrated in figure 39. One FBG was mechanically decoupled, by housing within a capillary tube, in order to measure the temperature directly; the other was embedded directly similar to the LPG. To ensure the fibres were straight and with even strain before embedding, they were fixed with tape at both ends, before applying the adhesive. The adhesive was cured with a standard production cure cycle.

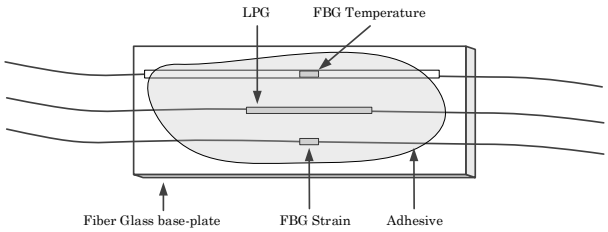


Figure 39 – Illustration of base-plate with gratings, from [108]

During the curing process, the strain-effects were investigated with the two co-located FBGs. Using the mechanically decupled FBG as temperature sensor, the temperature influence was subtracted from the strain sensor. The maximum strain during curing was below -30 με (-0.04nm). Indicating that strain effects during cure are small/negligible and therefore the maximum strain during curing does not contribute towards a significant change in the LPG spectrum. However uneven strain on the LPG can have an impact.

After curing, the embedded gratings were subject to a temperature test in the ranges 20.8 to 87.0 °C, due to maximum expected operating temperature and available equipment. Figure 40 shows the spectra of the LPG at minimum and maximum temperature. The depth of the LPG response has increased by only 0.14 dB, similar to observations for FBGs [7]. A negligible change of the FWHM was measured from 11.0 to 10.9 nm. This indicated a uniform strain/stress influence from the adhesive under temperature changes, which is of significant importance for providing a spectral-response/shape suitable for sensing.

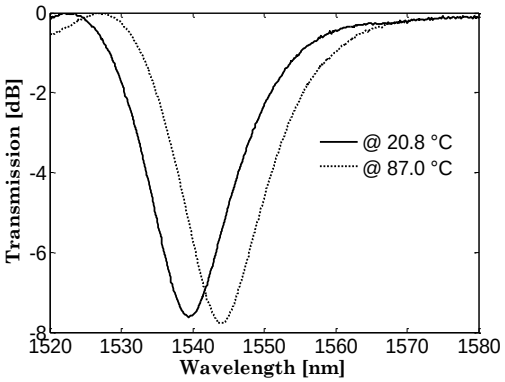


Figure 40 – Normalized spectra of LPG at minimum and maximum temperature, from [108]

The spectra were fitted to a polynomial and figure 41 shows a plot of the centre-wavelength against the temperature, including a linear regression line. The spectral shift of the centre wavelength are approximately 6.8 nm/100°C and with a linear response ($R^2$ = 0.995). The typical shift for a standard LPG is about 5-15nm/100°C [6]. These results illustrate good compatibility in expansion between the adhesive, the recoating material and the optical fibre, as the shift are within the limited for a typical LPG and the response are linear. Over the 66.2 °C temperature range, the FBG strain sensor shifted 1.38 nm (corrected for temperature shift), utilizing equation (2), this corresponds to approximately 1100 με. The FBG sensor for temperature sensing measured a shift of 0.59 nm, indicating that the expansion coefficient of the cured adhesive/baseplate has most influence of the wavelength shift on the FBG due to the longer shift.

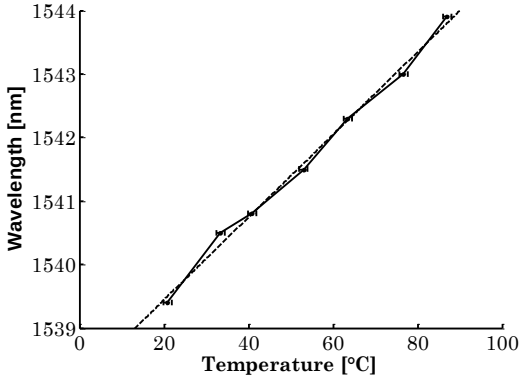


Figure 41 – Temperature response from embedded LPG, from [108]

**Discussion**

It is essential that a LPG sensor can be embedded in a process suitable for implementation in the wind turbine blade production. Successful embedding of LPGs directly into the adhesive utilized in the matrix of a wind turbine blade was here demonstrated. Embedding of FBGs was straight forward with negligible influence from the adhesive. LPGs however differ from FBGs and require a suitable recoating material, otherwise the spectrum is broadened and/or wavelength shifted. The strain during the cure process and strain during temperature drift was investigated. Only a small influence of strain during curing was measured, however a recoating is required to avoid micro-bend loss on the LPG and to ensure proper RI of the surroundings of the LPG. After curing the expansion coefficient of the adhesive/baseplate has influence of the change in wavelength of the embedded sensor. Moreover, the spectral response of the LPG retains its shape and has a linear response to temperature changes with sensitivity still in the range of a typically LPG, illustrating good compatibility for embedding LPGs. It is of significant importance that the shape, of the spectral response, is retained to provide a reliable load sensor based on LPGs. This has been verified during these experiments.

The selected recoating material is designed for industrial use in draw towers and has excellent peel strength on glass, which is critical for this application as a long life-time is required (20 years) in an environment with large temperature cycles (summer-winter). Therefore this recoating can avoid cracks or loosen recoating, which is critical as repair of an embedded sensor is not possible. For a commercial sensor the recoating process can be performed automaticity insuring an even recoating process [109]. In a development project this recoating would be subject to lifetime and extreme testing, and a slight change in the properties of the recoating material might be required for optimization e.g. tacky.

## 4.2 Characterisation of Optical Sensors

### Modelling – Mode Profiles and Couplings

A relatively simple qualitative model to describe the sensor and the resonance wavelengths for the couplings between the modes was created, to understand the sensing mechanism in greater detail. The model is based on experiments and describes the TE-TM_like couplings between the core- and claddings-modes, to predict the resonance wavelengths in the spectrum, including the ones outside our detection equipment range. To measure the mode-profiles in the D-shape fibre, *sensor 3* was cleaved at the end of the second grating and mounted in front of an infrared camera, with a collimation lens (x20 microscope objective) between the cleaved fibre end and the camera [91]. The mode-field patterns, in transmission, were measured when launching a 2 mW tuneable laser source into the fibres through the SMF-28 fibre (~ 1550 nm, resolution: 0.1 nm step size, 100 kHz line-width). Figure 42 shows primarily excitation of the core-mode at 1494 nm and figure 43 shows primarily excitation of the cladding-mode at 1509 nm. In both figures the flat-side is located at the top (away from the viewer) near the edge of the mode-profiles.

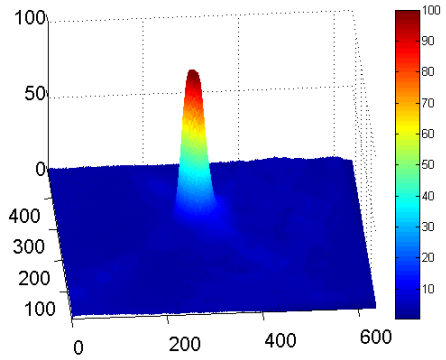


Figure 42 – Core-mode in D-shape fibre 1494 nm, from [91]

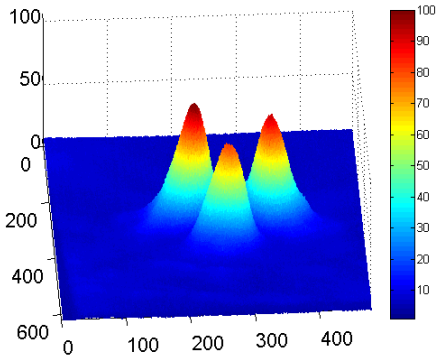


Figure 43 – Cladding-mode in D-shape fibre 1509 nm, from [91]

Based on the data in figure 42 and figure 43 the intensity distribution of the modes in the core, cladding and air can be approximated. Figure 44 shows a cross section of the core-mode intensity perpendicular to the flat-side. The left side is

towards the flat-side; note the mode is squeezed on this side, compared to the side away from the flat-side. From chapter 3.2 it is known that the MFR is 5.4 µm and that the core radius is 4.2 µm. With the measured profile and the MFR (intensity ~ 13.5%), it is estimated that about 80 % (± 2%) of the mode intensity is in the core region and the rest is in the cladding and air. With a distance from MFR to the flat-side of 2 µm it is estimated that the portion of the light in air is very low, and therefore close to 20% of the rest is in the inner cladding. The absolute portion of light in the core and cladding is less critical than the portion in air due to the much higher RI difference from silica to air than between the core and cladding.

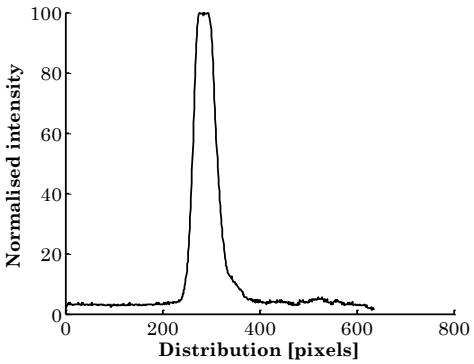


Figure 44 – Normalized core-mode intensity perpendicular to the flat-side, distribution in pixels

Based on the cladding-mode profile it is assumed that all three intensity peaks have about 3-4% of the intensity in the core (10% total), and close to 90% in the inner cladding. It is assumed that the portion of intensity in air, from the mode peak away from the flat-side, is negligible. When the bulge at the flat-side is taken into consideration (see figure 18), and the fact that the cladding-mode is not nearly as well confined as the core-mode, the portion of the intensity of the cladding-mode in air is assumed to be about the same as for the core-mode.

As an approximation the TE-like mode (polarization) have the E-field parallel with the surface of the flat-side and the TM-like mode are perpendicular to the surface of the flat-side [110]. From Maxwell's equations and the boundary conditions for TE- and TM-like, the change in the normal components of the D-field ($D=\varepsilon E$) across an interface should equal the surface charge density. Here both materials

(silica and air) are dielectric materials without any significant electrical potential difference, thus the surface charge can be approximated to zero. Therefore $\varepsilon_1 E_{n1}=\varepsilon_2 E_{n2}$, here the relative dielectric constant of silica is $\varepsilon=n^2\approx 2$ and for air it is 1. Therefore the TM-like field in air can be approximated as follow:

$$\text{TM-like\_}_{\text{cladding}} = \left(\frac{n_{air}}{n_{cl}}\right)^2 \text{TM-like\_}_{\text{air}} \tag{15}$$

Where $n_{air}$ and $n_{cl}$ are the RI of the air and the cladding, 1 and 1.44815 respectively. Therefore the E-field is 2 times larger in air, than in the cladding, and the intensity is 4 times larger for the TM-like mode. The E-field decreases exponentially away from the interface (and the exponential tail is very short due to the large index step) [110]. As mentioned the TE-like mode is considered to have the E-field parallel to the surface (intensity distribution in the material is assumed the same). Therefore there are no changes in the field and intensity over the interface, hence the intensity for the TE-like mode in air is, as an approximation, 4 times smaller than the TM-like mode.

Here the cladding modes are assumed to be all in the inner cladding, based on the mode-profiles in figure 42 and 43, the cross section in figure 18 and the profile index in figure 14, where it can be found that the distance from the edge of the inner cladding and to the core center is about 35 μm.

With the above assumptions a parameterization can be done as follow:

| Parameterization of intensity for first cladding mode | | | |
|---|---|---|---|
| | Intensity in core | Intensity in cladding | Intensity in air |
| $\text{TM-like}_{\text{core mode}}$ | 0.8 | $0.2\text{-}1 \cdot \eta$ | $1 \cdot \eta$ |
| $\text{TE-like}_{\text{core mode}}$ | 0.8 | $0.2\text{-}1/4 \cdot \eta$ | $1/4 \cdot \eta$ |
| $\text{TM-like}_{\text{cladding mode}}$ | 0.1 | $0.9\text{-}1 \cdot \eta$ | $1 \cdot \eta$ |
| $\text{TE-like}_{\text{cladding mode}}$ | 0.1 | $0.9\text{-}1/4 \cdot \eta$ | $1/4 \cdot \eta$ |

Table 4 – Parameterization of first cladding mode

Where $\eta$ is the portion of intensity in air. To find the resonance wavelength for the couplings from core- to cladding-mode, the part of intensity in each 3 regions are multiplied with the given RI respectively (1.48271, 1.44815, 1). For the coupling from the $\text{TM-like}_{\text{core mode}}$ to $\text{TE-like}_{\text{cladding mode}}$ the difference in the effective RI is as follow:

$$
\begin{aligned}
&0.8\cdot 1.45271+\left(0.2-\eta\right)\cdot 1.44815+\eta \\
&-0.1\cdot 1.45271+\left(0.9-\frac{1}{4}\eta\right)\cdot 1.44815+\frac{1}{4}\eta \\
&\Updownarrow \\
&\Delta n_{eff}=0.0031927-0.3361125\cdot\eta
\end{aligned}
\tag{16}
$$

Using equation (4) $\Delta n_{eff}$ is found to be 0.0025 for a dip at 1509 nm and with $\Lambda$ = 600 µm. Therefore $\eta$ is found to be ≈0.2%. Thereby 0.2% of the core-mode is in air (and 0.05% of the cladding mode is in the air for the TM-like – TE-like coupling. The other couplings are not physically possible with $\Lambda$ = 600 nm, as it requires the RI of air to be negative. For η ~0.2%, the other couplings have resonances between 1900-2300 nm (out of the spectral range of our detection equipment). As previously mentioned in chapter 3 it has been verified in the lab that there was no LPG for a 300 µm period, and therefore this cannot be a solution for the couplings (e.g. $\Delta n_{eff}$ ≈ 0.005). The RI of air is much lower than the cladding and core RI, therefore only small changes of the portion of the light intensity in air, gives large changes on the resonance wavelength e.g. a 10% relative change in the portion of light in air corresponds to a change in wavelength of 15 nm for the TM-like – TE-like coupling. For a coupling to a TM-like cladding mode, the sensitivity would be increased due to larger distribution of light in air.

During profile measurements there was a tendency to see an extra cladding-mode near 1560 nm on the monitor. As seen in figure 29, there is a weak second resonance dip at this wavelength. This mode was with positive amplitude on the left side of the core and with negative amplitude on the right side of the core (asymmetrical field distribution). However it was not possible get clear excitation of this cladding mode, but figure 45 indicates a mode with positive amplitude on left side possibly due to interference with the dominant cladding mode.

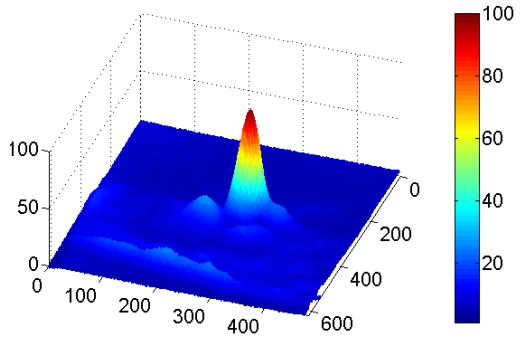


Figure 45 – Second cladding mode in D-shape fibre

Based on the same assumptions as for the first cladding-mode, geometry and mode confined such a cladding-mode profile is roughly estimated to have about 100% more intensity in air, and about 30% less intensity in the core, compared to the first cladding mode, and is parametrized as follows:

| Parameterization of intensity for second cladding mode | | | |
|---|---|---|---|
| | Intensity in core | Intensity in cladding | Intensity in air |
| TM-like$_{\text{Cladding mode}}$ | 0.07 | $0.93\text{-}0.5 \cdot \eta$ | $0.5 \cdot \eta$ |
| TE-like$_{\text{Cladding mode}}$ | 0.07 | $0.93\text{-}2 \cdot \eta$ | $2 \cdot \eta$ |

Table 5 – Parameterization of second cladding mode

For this cladding-mode all fundamental resonances are above the 1500 nm range. However the TE-TM-like coupling is about 3000 nm, and therefore it would have a second-order side resonance in the 1500 nm range (these are weak compared to the fundamental). The absolute wavelength is difficult to quantify as only 10% change of the intensity in air corresponds to a 100 nm change in the resonance wavelength. The first cladding-mode has a symmetrical field distribution and the second cladding-mode an asymmetrical, therefore the overlap integral is very small, hence the coupling between them is negligible.

The spectrum of *sensor 1* has been investigated from 1100 to 1700 nm, with both tunable lasers and broad band light sources, to find the second cladding mode.

Figure 46 show the spectrum using a broadband light source (MenloSystems TC-1550-B). Cut-off to multimode is seen about the predicted 1250 nm wavelength (chapter 3.2). No second cladding mode outside the first resonance at 1560 nm was observed; hence the resonance dip is very small and not possible to observe or it is out of the detection equipment range. The dips at 1400 nm are due to gas absorptions inside the OSA.

If the sensor is recoated before embedding, $n$ would be changed by the RI of the recoating material for the TM-like mode, due to the continuity of the D-field. For the TE-like mode $n$ changes by approximately $RI^3$ due to Maxwells equations and the above assumptions. Using this on the two cladding-modes for a recoating material with a RI of 1.37, the change for the first cladding-mode would be up to 15 nm and for the second cladding-mode the change would be several hundred nm.

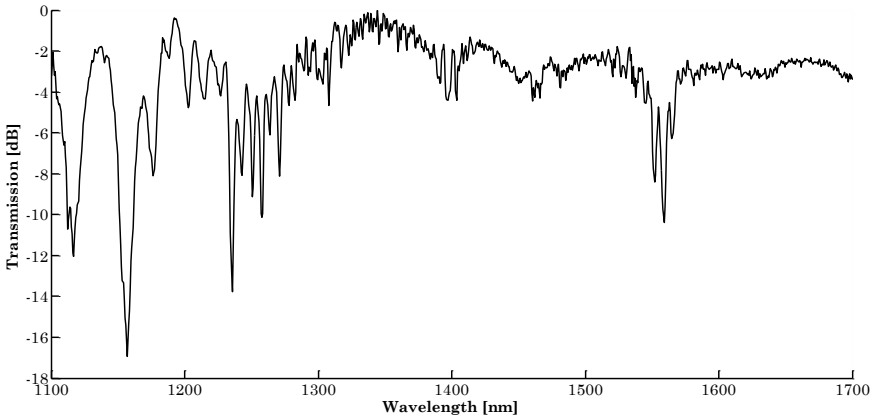


Figure 46 – Normalized broadband spectrum of *Sensor 1*

**Bending of Uncoated Fibre Sensor**

To characterise the LPG sensors regarding bending response, *sensor 2* was mounted in fibre holders placed on an optical table, see figure 47. Both holders was able to rotate the fibre 360°, and they were placed on micrometre-screws, such that the fibre could be moved and rotated to be characterised in all directions at given curvatures. A microscope (on a slide) was used to ensure orientation of the flat-side of the fibre and to avoid twisting. The curvature for the fibre in this setup is given by [111]:

$$R = \frac{2 \cdot d}{\left(d^2 + L^2\right)} \tag{17}$$

Where $L$ is the half distance between the edges of the two holders and $d$ is the bending displacement at the centre of the sensor. A digital camera and graph-paper was used to measure the bending displacement.

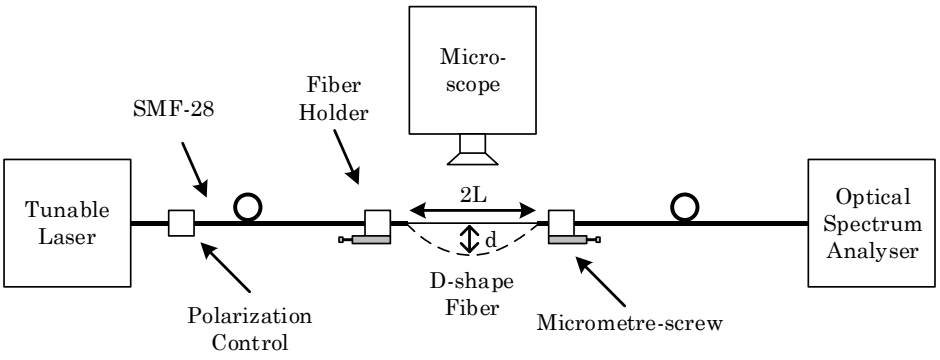


Figure 47 – Setup for curvature measurement of uncoated fibre

First the polarization control was used to measure the wavelength shift for the different polarizations. For the fiber to be birefringence, the flat-side must be very close to the core [112]. Here only a negligible wavelength shift was observed, however the depth of the dips are extremely sensitive which is in good agreement of the modeling, as it must be optimized for the TM-TE_like coupling.

The fiber was aligned with the flat-side upwards against the microscope and the polarization control was tuned to optimize the dip near 1557 nm. With the right optimization the dip at 1555 nm becomes rather strong, see figure 45. At figure 28 (measured with an unpolarised ASE) the dip at 1555 nm only has depth of less than 1 dB. It was checked that only a very small/negligible wavelength change occurred when a high temperature was applied on the D-shape fiber between the splice-point and the grating, and it was only the dip at 1557 nm that was subject to a change, thereby the dip at 1555 nm is not due to Fresnel reflection. The separation between the two dips is not consistent with the calculated separation of 5.4 nm (or the half). As described in the model (see chapter "Modelling – Mode profiles and coupling"), a side resonance can be in the 1500 nm range, where just a small change in the intensity in air shifts the resonance wavelength a lot. It is likely that on *sensor 1* the second cladding mode is out of the spectra or too small to distinguish from noise. However for *sensor 2* the 1555 nm dip is expected to come from the second cladding-mode. Therefore the response for the two dips was investigated.

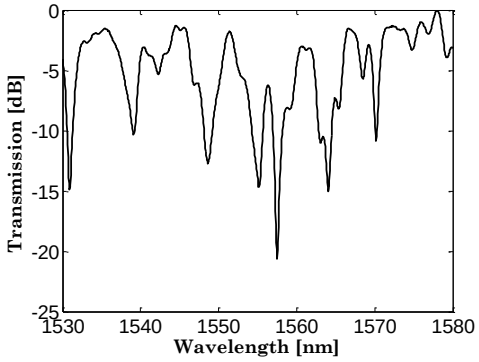


Figure 48 – Normalized spectrum of *Sensor 2,* optimized with polarisation control for the dip at 1557 nm

Figure 49, 50, 51 and 52 illustrates the wavelength shift at given curvatures for the two dips, 1555 nm and 1557 nm respectively. The sensor was bend in the two directions, flat-side up and down. For the direction perpendicular to this, the fibre twisted and a reliable measurement was not possible. Due to the read-out of the curvature, and that the un-coated (naked) fibre was sensitive to temperature changes, the error bars are large. It is seen that when bending with the flat-side down, the shift is linear, and when bending with the flat-side up the shift is more

exponential. Moreover, for curvatures under the maximum bend of a wind turbine blade (0.01 $m^{-1}$) the sensitivity is still rather linear. The dip near 1555 nm has a sensitivity of $-13 \cdot 10^{-9}$ $m^2$ for the flat-side up (towards microscope) and the dip near 1557 nm has a sensitivity of $-9 \cdot 10^{-9}$ $m^2$ (in the range up to 0.05 $m^{-1}$). For the round side up the sensitivity for the dip near 1555 nm is $18 \cdot 10^{-9}$ $m^2$ and the dip near 1557 nm has a sensitivity of $13 \cdot 10^{-9}$ $m^2$. The exponential sensitivity is largest for the 1557 nm dip, first cladding-mode (see chapter "Modelling – Mode profiles and coupling"). This mode has 3 intensity peaks, the peak on the opposite side to the flat-side influences this as it mode overlaps with the core-mode, and the overlap is different for bend the two directions. Due to intensity it is exponential.

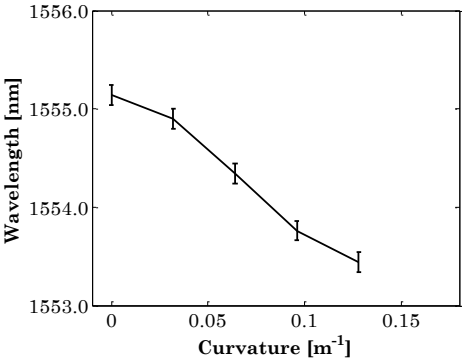


Figure 49 – Dip at 1555 nm for bend with flat-side up

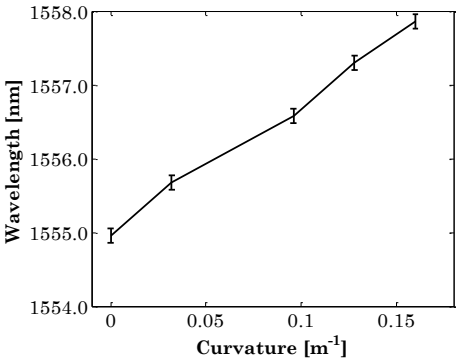


Figure 50 – Dip at 1555 nm for bend with flat-side down

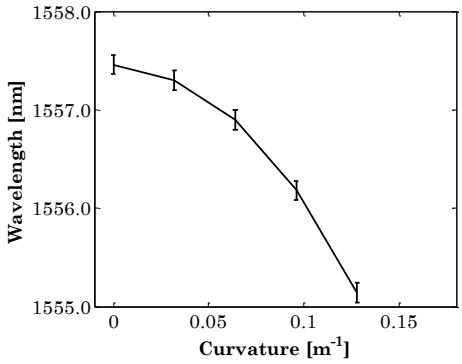


Figure 51 – Dip at 1557 for bend with the flat-side up

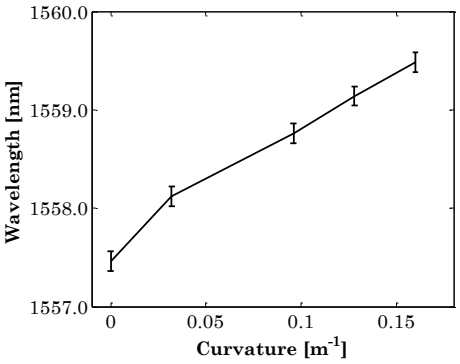


Figure 52 – Dip at 1557 nm for bend with flat-side down

The sensor was also investigated for strain response. The wavelength shift for positive strain was towards shorter wavelengths. As mentioned in chapter 2, this is affected by the change in period (longitudinal direction), strain optics (change in RI) and Poisson's ratio (transverse dimensions). The period change gives a contribution to a wavelength change towards longer wavelengths. The other changes contributes negative. The core in a fiber is soft compared to the cladding due to doping; therefore it has a larger expansion and different (negative) change in RI regarding strain and it contributes towards shorter wavelengths. For a D-shape fiber, the core can easier expand than in a standard fiber, therefore the contribution is larger, and the sensor have a strain response with wavelength shift towards negative wavelengths, due to $\Delta n_{eff}$. This is opposite to the wavelength shift for a FBG.

**Bending of Embedded Sensor**

*Sensor 1*, described in chapter 3.3, was embedded between two base-plates of fibre-glass. As the D-shape fibre was spliced to SMF-28 fibres, for connection during writing and re-splicing was undesirable (risk of damaged to the sensor), the D-shaped fibre could not be recoated with the setup described in chapter 4.1. First a 70 cm long and 2 cm wide fibre-glass base-plate was prepared with a 1 mm thick and 5 mm broad layer of cured recoating material. The D-shaped fibre was aligned with the flat-side away from the fibre-glass base-plate, at one end it was fixed with glue onto the SMF-28 fibre and at the other end elastic fixed on the SMF-28 ensured the D-shape fibre was straight and without twisting due to a small strain. Recoating material was carefully attached and cured with a small box where $N_2$ and UV-illumination was injected. Adhesive utilized in the matrix of a wind turbine blade was applied and a second base plate was attached. The embedded sensor was fixed on an optical table with holders at each end, 25 cm from the centre, ensuring two fix points for the embedded sensor to bend around, see figure 53. A micrometre-screw was used to bend the sensor and a dial gauge with a resolution of 1 µm was used for precise readout (see equation 17). Only a negligible change in FWHM and centre wavelength was observed, the model in the previous chapter predicted an up to 15 nm change, however it is also stated that only a very small change in intensity distribution in the surroundings shifts the wavelength similar.

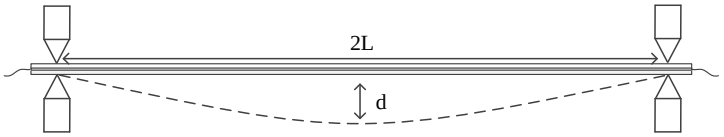


Figure 53 – Setup for curvature measurement on embedded sensor, from [104]

When an object is bending, there will be a compression on one side of the material (concave side) and an expansion on the other side (convex side). For small bends the elasticity (Young's modulus) can be assumed identical on both sides, and therefore equal on both sides, and there will be none compression or expansion in the middle of the object. As the two base-plates are identical and glued together, it can be assume to be one object, where the fiber is in the center, and it will therefore not be subject to strain, when the base-plate is bending.

In a pre-test for providing experimental knowledge about mounting, the sensor was attached on the outer-surface on a wind turbine blade at Vestas blade production facilities. The sensor was fixed with glue about 10 m from the tip of the blade and the blade was subject to a static bend to demonstrate a change in the wavelength of 0.16 nm. During removal the baseplate was damaged and the adhesive between the plates cracked. The sensor was repaired in the lab, and it was still able to function. However after the repair, the wavelength was subject to polarisation changes; see figure 54 showing maximum separation due to polarisation. The maximum shift is a few nm and is likely due to stress/twist on the fibre after the crack, as only negligible wavelength shift was observed before. This would also have an influence on the measurement when this sensor is placed on a wind turbine blade.

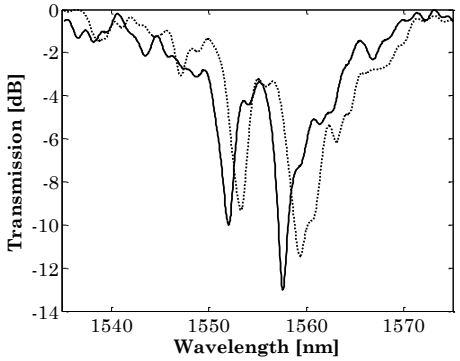


Figure 54 – Normalized spectra of maximum wavelength shift due to polarization

The embedded sensor was subject to bend in both directions (flat-side up and down). Figure 55 shows the resonance dips for different bends with curvature from 0.0 to 0.096 $m^{-1}$. The polarisation control was used to optimize the dip near 1558 nm. For bends larger than the maximum bend on a wind turbine blade (0.01 $m^{-1}$) the dip near 1550 nm, splits up into two dips. This was not seen for the non-recoated sensor and is likely to occur from the polarisation sensitivity after the crack, or strain due to the embedding. For the dip near 1558 nm, the sensitivity in both directions is $\approx 9 \cdot 10^{-9}$ $m^2$. This is slightly smaller than the uncoated fibre, and is either due to a small difference in the fibre parameter or the recoating/embedding (including the polarisation sensitivity).

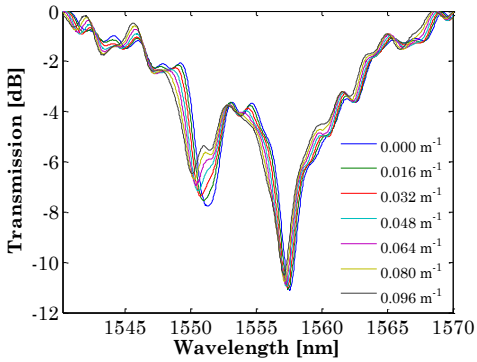


Figure 55 – Normalized spectra for different curvatures on embedded sensor

However the slopes of the dips shift with different sensitivity, this is clearly seen for the non-optimized dip at 1550 nm. Moreover this is negligible for bends below the maximum bend on a wind turbine blade for an optimized dip.

An important aspect is the resolution which it is possible to measure the wavelength shift with. Figure 56 shows spectra for wavelength shift for given curvatures and figure 57 plots the fitted centre wavelengths for the given curvatures. Since the publication [104] the setup has been optimized and the resolution able to be measured is ±1 pm. With a maximum bend of a wind turbine blade of 0.01 $m^{-1}$ and the measured sensitivity, the bend resolution of the blade of ~ ±1%, this is in the range of the requirements, requested by Vestas. This corresponds to a curvature resolution of ± 0.0001 $m^{-1}$

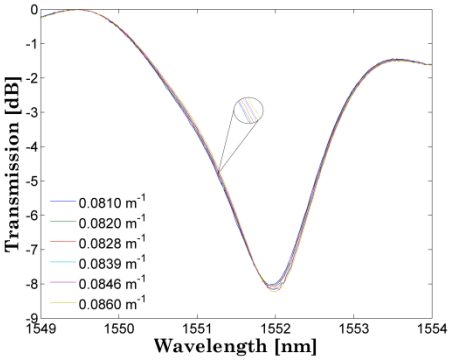


Figure 56 – Normalized spectra for curvatures with small steps

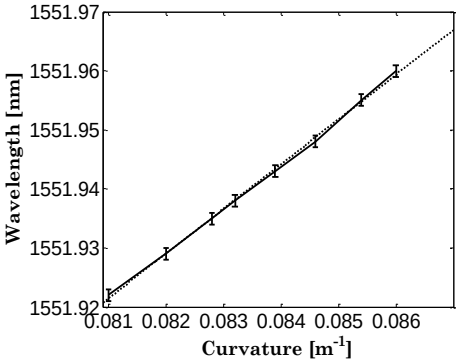


Figure 57 – Centre wavelength according to curvature

There is a negligible change in the FWHM of the dip, for curvatures up to 0.01 m-1. The embedded sensor was temperature tested and the sensitivity to temperature was found to be 4.1 nm/100C°, see figure 58. This is about 40 % lower sensitivity compared to the standard LPG embedded in chapter 4.1. However it depends on the fibre composition, grating composition and the embedding. This could be improved through a development project.

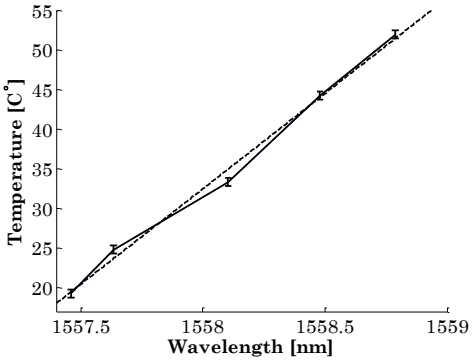


Figure 58 – Centre wavelength according to temperature for embedded sensor

**Discussion**

The three sensors described in chapter 3.3, have been subject to different investigations to provide a deeper knowledge and understanding of their mechanism. The mode-profile of *sensor 3* was measured and utilized to provide a model for the sensor type. This model provided a deeper insight about the sensor and the fundamental, TE-TM$_{_like}$ couplings, sensitivity to the different RI, interface from cladding to air/recoating, changes with recoating and absolute center wavelength. The model could be used to optimize the design or refine the sensor for future applications. From the model it is described that just a very small change of the light in the surroundings has a high impact to the resonance wavelength. More precise calculations can be performed with a mode-solver program, but it would only slightly contribute to deeper knowledge. Moreover, as the measured data, such as geometry of the fiber, is not known extremely precise the calculations would still have the same deviation as the model, therefore extensive lab work including several SEM (scanning electron microscope) and mode-profile measurements is required. The sensor is rather complex to design, with parameters such as RI of core, inner-cladding, outer-cladding and the surroundings (recoating), size of core, inner-cladding, outer-cladding and bulge, distance from flat-side to core-center, the selected coupling (TE-TM) and also the design of the gratings. Precise measurements of the parameters and simulations are required in the development phase to optimize the sensor for the given application. Furthermore, a design could include two inner-claddings, which might optimize the robustness, for more details see Appendix A [91].

The uncoated *Sensor 2* was subject to bend measurements. The sensor has more fringes than sensor 1, and the wavelength change between the dips was investigated. This shows different sensitivity for two dips, where the separation does not corresponds to the calculated separation of the MZ. It was demonstrated that the dips have different sensitivity depended on direction and resonance. The maximum sensitivity was $18 \cdot 10^{-9}$ m$^2$ which is about 50% better sensitivity than others have demonstrated [78]. Moreover, the bend sensitivity is much larger than the sensitivity achieved for a FBG, $0.77 \cdot 10^{-12}$ m$^2$ [45]. Utilizing the difference in sensitivity of the dips (two modes) the resolution of a sensor can be increased (Ratiometric) and also temperature and strain drift can be out-compensated (to first order) [73].

*Sensor 1* was recoated and successfully embedded into the adhesive material of a wind turbine blade. The characterization of the sensor reveals that the dip which was not optimized with the polarization control, splits up into two, but only for curvatures larger than the maximum bend of a wind turbine blade and is therefore not critical, moreover it was due to a crack between the base-plates and therefore not an issue for commercialized sensor. The sensor was subject to bending test and demonstrated a resolution of ±1 pm with a sensitivity of $\approx 9 \cdot 10^{-9}$ $m^2$, given a bend resolution of ~±1% with a linear response, which is as desired. The curvature resolution was ± 0.0001 $m^{-1}$, which is significantly better than others have demonstrated [78]. This sensor show no birefringence, others have utilized an elliptical core to make the D-shape fiber birefringence [79], this can for example be utilized to measure on both slow and fast axis and thereby out compensate temperature drift.

## 4.3 Test on a Wind Turbine Blade

### Installation on Blade

*Sensor 1* (embedded between two fibre glass base plates), was subject to load tests on an 80 m long prototype blade for the Vestas 8 MW V164 wind turbine [113]. The sensor was mounted inside the blade (flat-side against flap forward). At Vestas test facilities for prototype blades on Isle of Wight, UK. The blade was fixed on a test-rig, for static and dynamic tests of the blade. This test rig was able to test the blade in all directions, forward and reverse in both flap- and edge-wise directions, see figure 59.

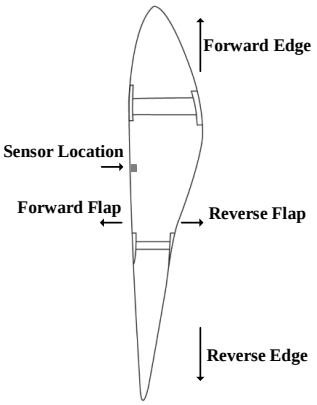


Figure 59 – Illustration of sensor placement on blade, from [113]

Due to the transportation and the availability, a setup with a broadband light source "DenseLight DL-CS5169A" and an "Ibsen I-MON 512 E" interrogator was selected. The interrogator provides 512 points over the spectrum (1510 to 1595 nm, ~6 sample points per nm) and is customized for FBG sensing and provides for FBGs a fitted resolution of 0.5 pm. The light source is a SLED and is polarised, therefore a polarisation control was utilized to optimize the spectrum. The light source has an optical power of 16 mW and it saturates the spectrum outside the dip, see figure 60. It was not possible to provide a suitable attenuator that was proven to be stable and with even attention over the spectrum. Therefore the saturation was accepted.

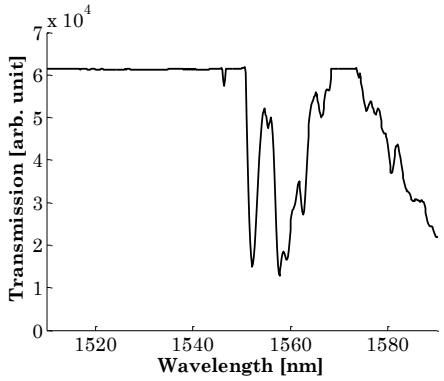


Figure 60 – Spectrum with interrogator and light source utilized for measurements on blade, from [113]

*Sensor 1* was fixed to the inside surface of the blade with an adhesive, normally used on prototype blades (optimized for strain transfer from the blade to a sensor), cables were fixed with glue and cable ties, see figure 61 (blue adhesive for fixing the sensor, white for cable fixing). The sensor was located near the optimum location for maximum curvature of the blade structure (when subject to load). For comparison, a FBG strain sensor was located within 2 m from the LPG sensor (but on opposite side of the natural axis), the FBG was interrogated with a commercial FBG sensing system from MOOG Insensys. FC/APC connectors were used to connect a duplex 50 m long SMF-28 cable and to the light source (with a polarisation control) and the interrogator, located on a table outside the blade, see figure 62.

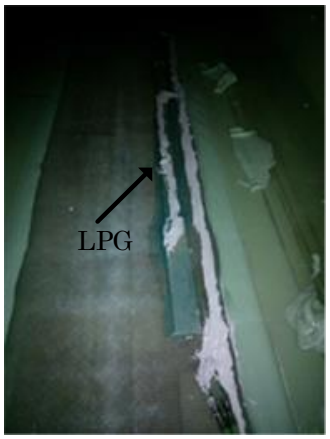


Figure 61 – LPG sensor fixed on the inside surface of the blade

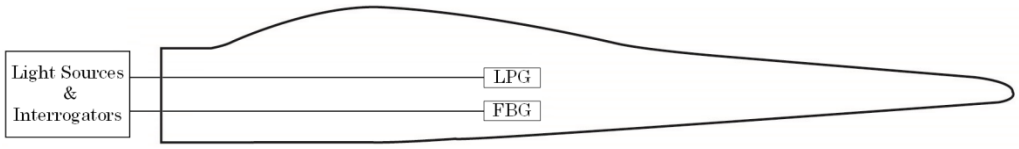


Figure 62 – Illustration of sensor and equipment placement

As the sensor is fixed to the blade, the deformation of the blade has influence on the measurement parameters; hence the measured parameter is a combination of strain, and bending onto the sensor. This is different from the lab setup, where strain was suppressed.

**Characterisation of Blade Noise**

The sensor was placed inside a wind turbine blade (34 ton), located inside a temperature controlled building, and a static test takes about 30 min, therefore temperature changes are negligible. Before the static load test while the blade was located in a position with the edge-wise side in horizontal position, and there was no activity at or near the blade, the "noise" was interrogated. The spectra were investigated and figure 63 shows the spectra from 10 samples with different time intervals between. It is seen that the spectra are almost identical. The dip was fitted to a $10^{th}$ order polynomial and the noise was analysed to be a wavelength change of maximum ~±3 pm, and it is expected mostly to be natural oscillation from the blade. Note that the output from the interrogator is linear and with arbitrary unit.

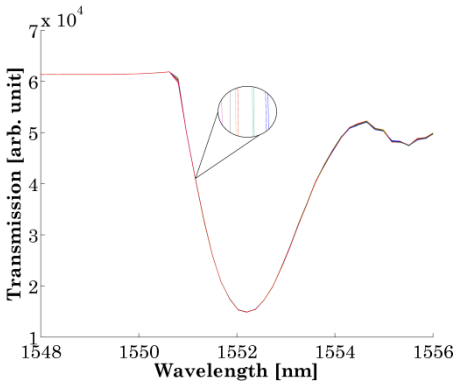


Figure 63 – Noise test on blade in edge wise horizontal position

**Static Test – Forward Edge**

The blade was rotated on the test rig to be in position for load testing in the forward edge direction of the blade. With winches and clamps along the blade, it was loaded to given set-points and held for a short time, first at 50 % (based on newton meters of maximum designed load). The initial start loads are calculated on the self-weight of the blade and the weight of the clamps (for a point located 1 m away from the sensor location). As the blade is not symmetrical (the blade is designed to take loads primarily in the forward flap direction), the initial loads are different for different orientations. As the start loads are calculated a slightly offset can be expected compared to the measured data. The spectrum was optimized for the dip near 1552 nm with the polarisation control before each test. To reduce complexity and thereby increase success rate, it was decided to only optimize for one dip and interrogate the wavelength shift of this. Figure 64 shows the dip at given loads for the forward edge test. It is seen that the sensor is subject to a very small change, the wavelength shift is towards longer wavelengths, recall from chapter 4, the sensor have opposite wavelength change compared to a FBG for longitudinal strain. Figure 65 shows the fitted centre wavelength according to the given loads (55 pm in total spectra shift).

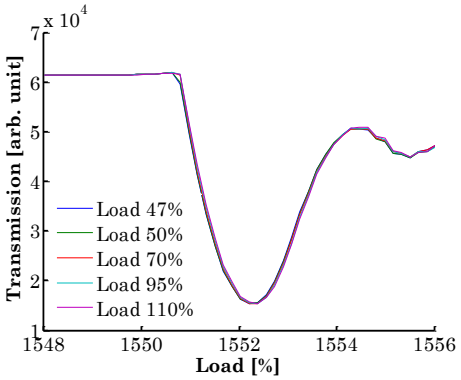


Figure 64 – Forward Edge: Spectra at different loads

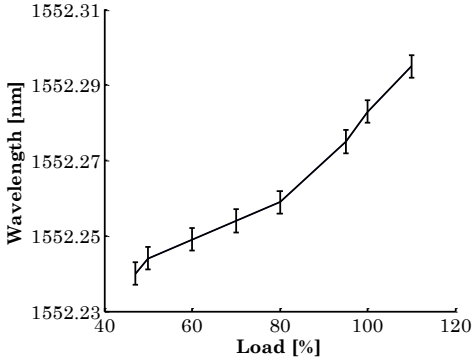


Figure 65 — Forward Edge: LPG centre wavelength compared to load

Figure 66 shows the fitted centre wavelength according to the strain measured with the FBG, at the given loads. It is clearly seen that near -300 με (90 % load) there is a change in the sensitivity. The change in sensitivity is due to overlap of the fields between the cladding and core-mode. Figure 67 compares the strain to the load, showing a linear regression of $R^2$=0.999, if the offset is neglected. Note no offset for the start loads when the two sensors are compared directly, figure 66. From 0 to -300 με the LPG sensitivity compared to the FBG is approximately 0.08 pm/με and above it is approximately 0.2 pm/με.

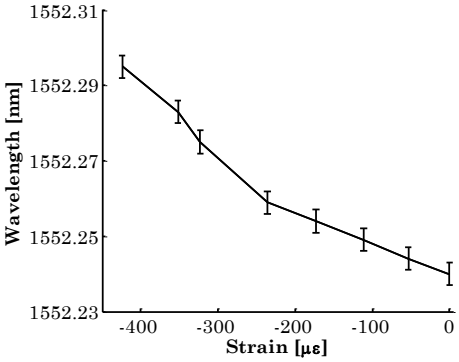


Figure 66 – Forward Edge: FBG Strain compared to LPG Wavelength at given loads

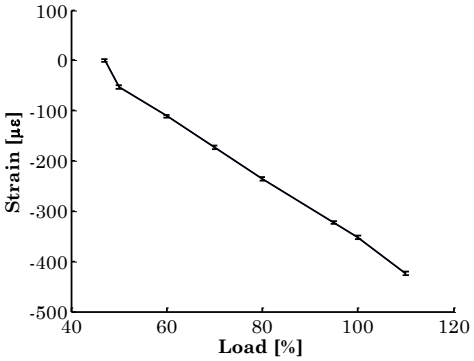


Figure 67 – Forward Edge: FBG strain compared to load

**Static Test – Reverse Edge**

Figure 68 shows the dip at given loads for the reverse edge test. The wavelengths are moving towards shorter wavelengths, opposite to the forward edge test. Figure 69 shows the fitted centre wavelength according to the given loads (-90 pm in total spectral shift).

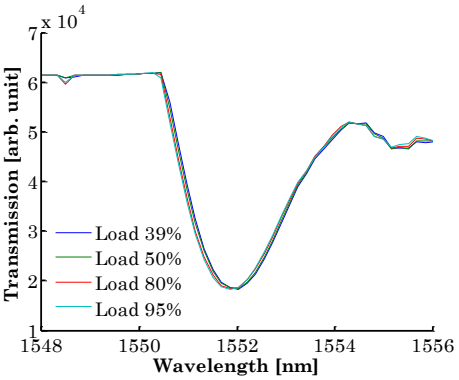


Figure 68 – Reverse Edge: Spectra from different loads

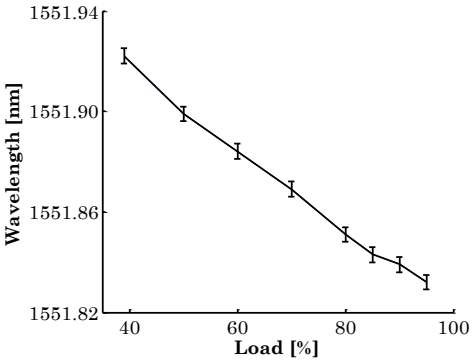


Figure 69 – Reverse Edge: LPG centre wavelength compared to load

Figure 70 shows the fitted centre wavelength according to the strain measured with the FBG, at the given loads. Again there is a small change in the LPG sensitivity about 300 με, however it is much smaller than for the forward edge test. From 0 to 300 με the LPG sensitivity compared the FBG is approximately -0.2 pm/με and above it is approximately -0.16 pm/με. Figure 71 shown the FBG strain compared to the load, the linear regression is $R^2$=0.998 (offset negligible).

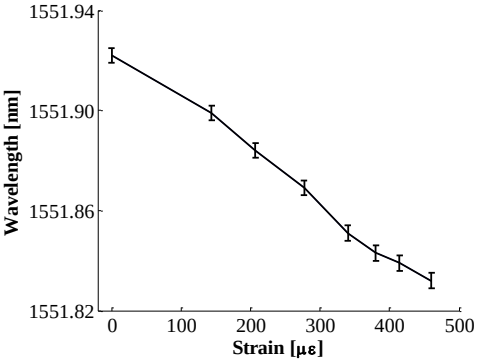


Figure 70 – Reverse Edge: FBG strain compared to LPG wavelength shift, from [113]

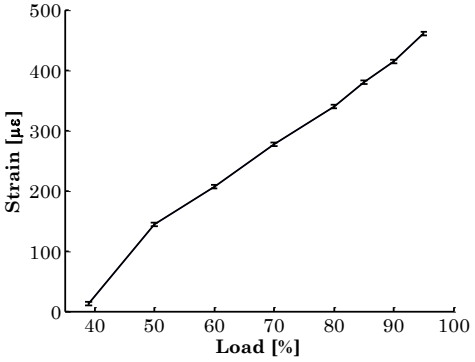


Figure 71 – Reverse Edge: FBG strain compared to load

## Static Test – Reverse Flap

Figure 72 shows the dip at given loads for the reverse flap test. The wavelengths are moving towards longer wavelengths. The wavelength movement is clearly seen and as expected much larger than for the edge wise bending, as the sensor is directional sensitive and the load in the flap directions is higher. Figure 73 shows the fitted centre wavelength according to the given loads (833 pm in total spectral shift).

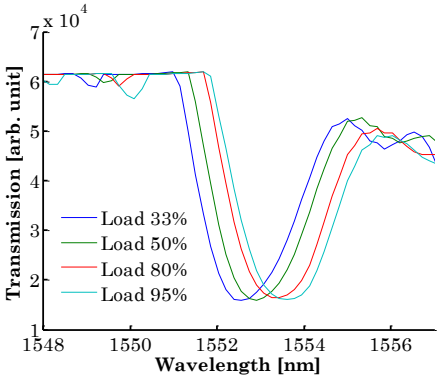


Figure 72 – Reverse Flap: Spectra from different loads

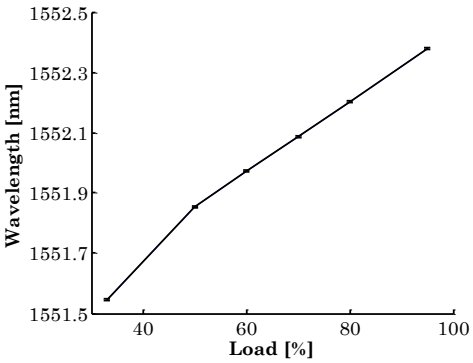


Figure 73 – Reverse Flap: LPG centre wavelength compared to load

Figure 74 shows the fitted centre wavelength according to the strain measured with the FBG, at the given loads. It is seen that there also in the flap direction is no offset when comparing the LPG centre wavelength to the strain, only for the comparison to the calculated start load. The sensitivity is approximately 0.99 pm/με (close to the typical 1.2 pm/με for a FBG, but with opposite sign). Compared to the edge wise bending the sensitivity is about a factor of minimum ~5 larger (maximum ~12). Different from the edge wise test, there is no change in sensitivity. Figure 75 shows the FBG strain compared to the loads ($R^2$=0.989).

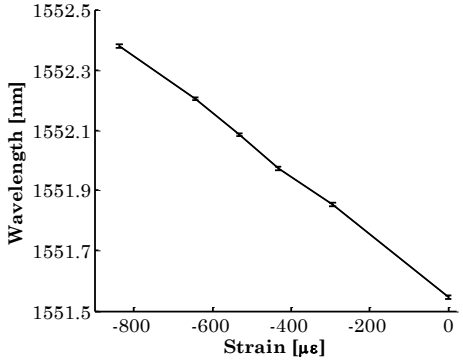


Figure 74 – Reverse Flap: FBG strain compared to LPG wavelength shift, from [113]

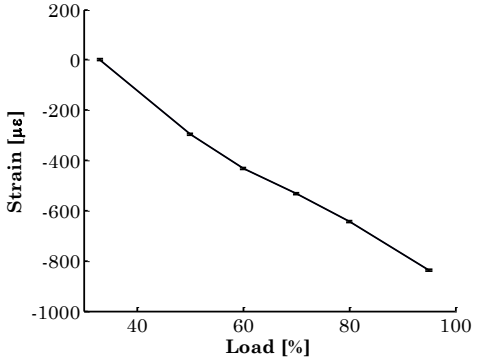


Figure 75 – Reverse Flap: FBG strain compared to load

**Static Test – Forward Flap**

During the flap forward test an issue occurred, see figure 76 (for transparency only spectra from 3 loads are shown). Likely the transport fibres were twisted while rotating the blade to the flap forward position. Therefore there was a significantly drop in transmission power, and possibly a change in the polarisation. Furthermore the FBG sensor suffered a critical error just above 95% load where the optical power was lost (due to a mechanical splice failure).

Measuring on the left slope of the dip, the change in wavelength from 19% load to 95% load is -2127 pm, and for the FBG the change is 1546 με, giving a sensitivity of -1.37 pm/με. However this is with some uncertainty, due to the cabling issue

under the test. But compared to the reverse flap test this is indicates that the sensor might be about 37% more sensitive in the flap forward direction. The sensitivity is minimum a factor of ~7 times larger than edgewise (maximum ~17 times).

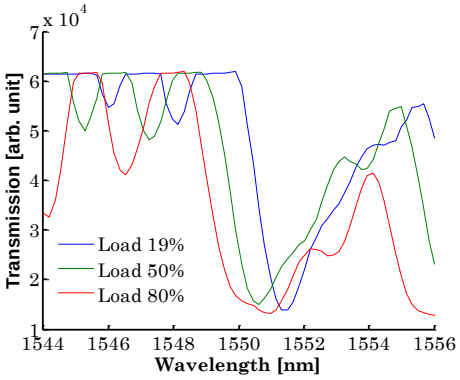


Figure 76 – Forward Flap: Spectra from different loads

**Discussion**

A full scale-test of the sensor on a prototype blade for a Vestas V164 wind turbine (80 m, 34 ton) was conducted. In general the test was very successful, and all concepts were proven. The light source and interrogator used for the test was not optimized with the sensor, saturating the spectrum outside the dip, however the resultant data from the tests were useful for proving the concept. For a production ready sensor, a better matched light source and detector can be selected or customized.

It was decided to use standard optical fiber between the sensor and to the interrogator/light source, as this may be expected in a final sensor solution, and therefore would provide knowledge about practical deployment issues. This sensor was, due to previous preliminary testing, damaged and found to be polarisation sensitive and another solution would be to use a polarization maintaining fibre along the blade, such as panda or bow tie fibres; they are more costly and would not be used in a final sensor, where the fibre is embedded directly into the blade material, providing high stability and the issue with twisting as in the test here would not be a problem. Moreover, the polarisation sensitivity was negligible

before the sensor was damaged, and therefore the sensitivity in a commercial one would not be an issue. The test setup prevented the measurement equipment to be located as close as possible to the sensor which would have reduced these effects.

During download of the blade only negligible hysteresis was observed. Due to the cable issue at the flap forward test the fiber between the sensor and the interrogator and light source was checked, but it was not possible to quantify a specific error. However the glue near the FC/APC connectors was repaired before the dynamic test. Note that the flap forward test imparts the most strain on the sensor; however the issue occur from the start of the test, so it is unlikely that it is due to more strain than in the edge wise and reverse flap test. Moreover it is likely the issue was due to a twisting of the cable while turning the blade around and the twisting was affected by strain when the blade was bending.

With a maximum curvature of 0.01 $m^{-1}$ (when the blade is at 100% load) and a bend sensitivity of $9 \cdot 10^{-9}$ $m^2$, a maximum wavelength change due to bend is about 90 pm. In the flap tests the wavelength changes was much larger (800 and 2000 pm), in such a test on a wind turbine blade the sensor is subject to both strain and bend, it is here demonstrated that the strain sensitivity for this sensor have highest sensitivity. For a commercial sensor this can be optimized, such that the bend and stain add to provide as much sensitivity as possible. As mentioned in chapter 2 & 4 the fiber composition and the grating period influences the sensitivity to strain and temperature, this can also be taken into account when optimizing the fiber. Such that strain and/or temperature is out compensated and the sensor measure the bend directly.

The sensor demonstrated a suppression of the edge-wise load of a factor between ~5 and ~17 times, depended on direction and curvature. Here the sensor differs from the typical FBG which are equally sensitive in all directions and requires extra sensors with different orientation to provide the same functionality. A very interesting aspect is the change in sensitivity, shown at the edgewise test. This might have possibility to either enhance the sensitivity to a given direction or suppress it e.g. with a pre-bend sensor, or with utilization of two sensor with opposite properties (one pre-bend and the other one straight) to out compensate temperature or strain. This requires future research and development of the fiber to provide the optimum geometry and mode profile, such that a better suppression is possible. The response of the sensor differs for the forward and reverse directions. This is due to the overlap of the mode profiles, and it is also affected by

small difference in the fiber and location on the blade. Moreover the sensor can be designed such that the overlap between the field of core- and cladding-mode is optimized, such the selectivity can be further increased. This can be of significant importance, to suppress edge wise bending, providing less complex software due to a selective sensor. Future research and development can be based on exploring further functionality of the change in sensitivity e.g. with a number of identical sensor at different locations and orientation around the neutral axis on the blade.

Recall from chapter 3.3, *sensor 1* is in total about 20 nm broad. As the D-shape fiber is single-mode from 1250 nm and the transport fiber has a relative short length and thereby loss is negligible (~100 m), the entire telecommunication band from 1260 to 1675 nm (O- to U-Band) can be used. With an overall width of 20 nm as *sensor 1*, applications with up to 20 sensors is possible, this can further be increased with optimization such as apodizing (suppress side modes). In chapter 2 it was stated that 2 to 16 FBG sensors is required depended on application. As this sensor is selective a lower number can be expected, and up to 8 sensors is likely. With optimization a wavelength range of 100-150 nm can be expected to be interrogated, which is possible with typical telecommunication equipment. With a typical FBG detector, as the one used in these tests, about 6 sensors can be possible in one fiber, which is enough in most applications due to the selectivity of this sensor.

As mentioned, systematic errors can come from edge wise bending and temperature drift, where this sensor have the advantages to passive out compensate this though the design. However errors due to noise also need to be considered, such as amplitude noise from the light source, detector noise, common-mode rejection, temperature and shot-noise. Shot-noise would be a bit larger for LPGs due to transmission, but would also provide more signal power to the detector. Moreover all this can be sufficient suppressed with commercial interrogator systems for FBG, which can be used for LPG detection as we have similar detection bandwidth and resolution requirements, also demonstrated in the tests on the wind turbine with a LPG sensor, given good quality of the measurements. But the FBG cannot suppress the edgewise bending, and here this LPG sensor has great advantages.

The dynamic testing of the blade was not started before the submission of this thesis, but is subject to future investigation of the sensors capability.

# 5. Conclusion

The work described in this thesis covers the research preformed within the field of fibre-optical load sensors for wind turbine blades. The project was based on the idea of utilizing asymmetrical fibres and Long-Period Gratings (LPGs) as a novel load sensor for wind turbine blades. The objective was to perform applied research with LPGs demonstrating a competitive sensor technology to the traditional Fibre Bragg Grating (FBG) sensors and with much better selectivity sensing properties. The field of utilization of LPGs as sensors on wind turbine blades is new and this project has provided a review article on fibre grating sensors in wind turbines [108]. In addition the project has provided research regarding embedding of LPGs, in particular using special D-shape fibre, in the adhesive utilized in the matrix of a wind turbine blade and testing of these sensors on a full-scale wind turbine blade, and foresees the potential use of this technology in the future.

## Results

Different asymmetrical fibres were investigated for this application, and a D-shape design was selected. Where other asymmetrical fibres such as those with Core-Concentricity-Error have a difficult and costly alignment process, a D-shape fibre has great advantages for easy alignment utilizing of the flat-side of the fibre, which is of significant importance for commercialization of the sensor. Furthermore D-shape fibres are also easier to manufacture with the typical Modified Chemical Vapor Deposition (MCVD) and draw tower process. To provide a fibre with the specific properties required for this application, a D-shape fibre was specially fabricated as part of this project. A preform was manufactured with a MCVD setup, and the preform was milled down to a D-shape before drawn on a customized draw tower setup. This provided a number of D-shape fibres with different core-centre to flat-side distance. The most suitable one was selected and LPGs were written in the fibre using a UV-laser setup. LPGs have a large bandwidth, especially compared to FBGs, which limits the effective measurement resolution. To optimize the effective resolution a design with two LPGs acting as a Mach-Zehnder interferometer was selected, proving narrow fringes and suppression of noise.

The sensors were characterised in the lab for bending of the uncoated fibre. Sensitivity up to 50% larger than demonstrated in the literature was achieved, dependent on the selected fringes/resonance dip and direction. The mode-profiles of the sensor was characterised with an infrared camera, to provide deeper knowledge about the sensor. Together with the geometry of the fibre a model explaining the coupling between modes was established. The model describes the resonance wavelengths and how critical the portions of light in air/recoating is for the given mode.

A critical aspect of the sensor is the embedding into the matrix of a wind turbine blade. To provide the best robustness and lifetime it is desired to embed a sensor directly into the matrix of a wind turbine blade. Experiments were performed to investigate this possibility. It was clearly demonstrated that the properties of the LPG sensor must be matched to the adhesive, otherwise the spectral resonance is broadened and the dip decreased so the spectral response is insufficient for sensing. This is due to the RI and micro-bending of the adhesive utilized in the wind turbine blade. It was demonstrated that with utilization of a suitable recoating material and process only a negligible change in the characteristics of the resonance occurred. The recoating must be applied correctly to avoid a compromised spectrum. The embedding method showed a linear response to temperature changes without spectral changes. This is critical given the environment wind turbines are located in. The sensor was subject to bend-testing in the lab, and showed a bend sensitivity of $\approx 9 \cdot 10^{-9}$ $m^2$ with a resolution of ±1pm. Compared to traditional FBG sensors, this sensitivity is at least a factor of 10 times larger. It provides a bend sensing resolution of ~±1 % of the maximum curvature for a wind turbine blade, with a curvature resolution of ± 0.0001 $m^{-1}$, which is significantly more than others have demonstrated. Additionally the sensitivity to temperature was suppressed about 40%, compared to a standard embedded LPG.

A preliminary load test was performed on a production blade, where the sensor was fixed near the tip of the blade and subject to a bending load. The sensor cracked during posttest removal from the blade surface. However despite the sensor damage the recoating stayed on-to the fiber and it was possible to repair the sensor. This illustrated that the recoating (embedding) method was robust. The repaired sensor was subsequently fixed on the inside of a Vestas V164 wind turbine blade, and subjected to a standard set of static load tests. The sensor demonstrated very good performance and response. In this test the response is a

combination of bend, stain and stress (birefringence) on the sensor. The sensor provided comparable sensitivity as FBGs in the flap-wise directions, and was able to suppress the sensitivity to edge-wise bending with a factor of up to 17 times (minimum 5 times) depending on direction and curvature, due to the D-shape design. This differentiates the sensor from traditional FBG sensor and gives this sensor great advantage as a physical selectivity provides easier software-analysis of the readout.

In summary, the project has provided a novel prototype of an embedded LPG sensor which is capable of providing measurements with the required sensitivity and resolution. The sensor has been tested on a wind turbine blade demonstrating the capability of the sensor to survive in an industrial environment. Compared to traditional FBG sensors, this type of sensor has great advantages in selectivity to out-compensate edge-wise bending and also the possibility to out-compensate strain and temperature through the design. Additionally it can be designed to measure both strain and bend for maximum sensitivity.

## Outlook

This thesis covers the work done in the research-phase of the project. All major milestones were completed; fiber design/manufacturing, embedding, sensitivity/resolution, modelling, and test on a Vestas V164 wind turbine blade, all this provides crucial knowledge to the development phase. In the development phase a mode-solver software program can be utilized together with e.g. topology optimization or other systematic methods to optimize the sensor and give the most suitable sensor for the desired application. This can for example include selection of the best coupling between TE-TM modes. Suppressing the cross-sensitivity to strain and/or temperature with optimized grating, fiber and doping-design. However as a larger number of parameters influence the sensors, it requires extensive simulations and experiments and it requires an optical fiber manufactured from a commercial fiber facility with correctly controlled parameters from a sensing applications perspective and ensure reproducible fabrication.

The fibre design might be optimized for example by a combination of a D-shape and flat-side fibre to eliminate twisting of the fibre, and the size of the fibre might

be increased for easier handling. Another important part of the development phase is to select the most suitable light source and interrogator, which is driven by the number of sensors. Therefore it also includes system tests on blades to estimate the minimum required number of sensors, this might be different from the minimum required number of FBGs, as the bend can be measured directly (design dependent) and the sensor is selective. Furthermore, lifetime and extreme test is required before a commercial product can be available. Despite the fact the embedded sensor has proven to be very robust, it will require design changes to improve its performance and make it design-ready for manufacture. Others have demonstrated that this can be a critical aspect for FBGs [4].

# 6. References

[1] K. Chang-Hwan, P. Insu and Y. Neungsoo, "Monitoring of small wind turbine blade using FBG sensors," in *International Conference on Control Automation and Systems,* 2010, pp. 1059-1061.

[2] Better Plan: http://betterplan.squarespace.com/todays-special/tag/invenergy?currentPage=3, 05/02/2014

[3] B. F. Sørensen, L. Lading and P. Sendrup, "Fundamentals for remote structural health monitoring of wind turbine blades - a pre-project," Risø National Lab., Materials Research Dept., Roskilde, Denmark, 2002.

[4] K. Krebber, W. Habel, T. Gutmann and C. Schram, "Fiber bragg grating sensors for monitoring of wind turbine blades," in *Proc. SPIE 5855, 17th International Conference on Optical Fibre Sensors,* 2005, pp. 1036-1039.

[5] C. S. Shin, B. L. Chen, J. R. Cheng and S. K. Liaw, "Impact Response of a Wind Turbine Blade Measured by Distributed FBG Sensors," *Mater. Manuf. Process.,* vol. 25, pp. 268-271, 2010.

[6] A. Méndez, "Fiber bragg grating sensors: A market overview," in *Proc. SPIE 6619, Third European Workshop on Optical Fibre Sensors,* 2007, pp. 661905.

[7] Y. Chen, Y. Q. Ni, X. W. Ye, H. X. Yang and S. Zhu, "Structural health monitoring of wind turbine blade using fiber bragg grating sensors and fiber optic rotary joint," in *Proc. SPIE 8345, Sensors and Smart Structures Technologies for Civil, Mechanical, and Aerospace Systems,* 2012, pp. 834534.

[8] W. Ecke and K. Schroeder, "Fiber bragg grating sensor system for operational load monitoring of wind turbine blades," in *Proc. SPIE 6933, Smart Sensor Phenomena, Technology, Networks, and Systems,* 2008, pp. 69330.

[9] K. Schroeder, W. Ecke, J. Apitz, E. Lembke and G. Lenschow, "A fibre Bragg grating sensor system monitors operational load in a wind turbine rotor blade," *Meas. Sci. Technol.,* vol. 17, pp. 1167-1172, 2006.

[10] Moog: http://www.moog.co.uk/markets-overview/wind-energy/, 05/02/2014

[11] Fibersensing: http://w3.fibersensing.com/, 05/02/14

[12] Smartfibres: http://www.smartfibres.com/, 05/02/14

[13] HBM: http://hbm.com/, 05/02/2014

[14] M. Volanthen. "Placement of strain sensors in wind turbine blade," US8161822, 2012.

[15] M. Volanthen, P. M. Rhead, M. P. W. Jones and G. D. Lloyd. "Structural monitoring of wind turbine with fibre bragg grating sensors in each blade," US8545179, 2013.

[16] I. S. Olesen and L. Glavind, "System and method for identifying the likelihood of a tower strike where a rotor blade strikes the tower of a wind turbine," US20130287567 A1, 2011.

[17] J. Hübner, M. Kristensen and J. Rathje. "A sensor and a method for determining the direction and the amplitude of a bend," *WO2000070307 A3* , 2001.

[18] L. Glavind, I. S. Olesen, B. F. Skipper and M. Kristensen, "Fiber-optical grating sensors for wind turbine blades: a review," *Optical Engineering,* vol. 52, pp. 030901-1 - 030901-9, 2013.

[19] M. Yamada and K. Sakuda, "Analysis of almost-periodic distributed feedback slab waveguides via a fundamental matrix approach," *Appl. Opt.,* vol. 26, pp. 3474-3478, 1987.

[20] K. O. Hill and G. Meltz, "Fiber Bragg grating technology fundamentals and overview," *J. Lightwave Technol.,* vol. 15, pp. 1263-1276, 1997.

[21] R. Kashyap, *Fiber Bragg Gratings*. Academic Press, 2009.

[22] A. Othonos and K. Kalli, *Fiber Bragg Gratings: Fundamentals and Applications in Telecommunications and Sensing*. Artech House Publishers, 1999.

[23] T. Erdogan, "Cladding-mode resonances in short- and long-period fiber grating filters," *J. Opt. Soc. Am. A,* vol. 14, pp. 1760-1773, 1997.

[24] T. Erdogan, "Fiber grating spectra," *J. Lightwave Technol.,* vol. 15, pp. 1277-1294, 1997.

[25] A. D. Kersey, M. A. Davis, H. J. Patrick, M. LeBlanc, K. P. Koo, C. G. Askins, M. A. Putnam and E. J. Friebele, "Fiber grating sensors," *J. Lightwave Technol.,* vol. 15, pp. 1442-1463, 1997.

[26] K. O. Hill, Y. Fujii, D. C. Johnson and B. S. Kawasaki, "Photosensitivity in Optical Fiber Waveguides - Application to Reflection Filter Fabrication," *Appl. Phys. Lett.,* vol. 32, pp. 647-649, 1978.

[27] G. Meltz, W. W. Morey and W. H. Glenn, "Formation of Bragg gratings in optical fibers by a transverse holographic method," *Opt. Lett.,* vol. 14, pp. 823-825, 1989.

[28] K. O. Hill, B. Malo, F. Bilodeau, D. C. Johnson and J. Albert, "Bragg Gratings Fabricated in Monomode Photosensitive Optical Fiber by Uv Exposure through a Phase Mask," *Appl. Phys. Lett.,* vol. 62, pp. 1035-1037, 1993.

[29] M. Kristensen, "Ultraviolet-light-induced processes in germanium-doped silica," *Physical Review B,* vol. 64, pp. 144201, 2001.

[30] S. Bandyopadhyay, J. Canning, M. Stevenson and K. Cook, "Ultrahigh-temperature regenerated gratings in boron-codoped germanosilicate optical fiber using 193 nm," *Opt. Lett.,* vol. 33, pp. 1917-1919, 2008.

[31] P. J. Lemaire, R. M. Atkins, V. Mizrahi and W. A. Reed, "High pressure $H_2$ loading as a technique for achieving ultrahigh UV photosensitivity and thermal sensitivity in $GeO_2$ doped optical fibres," *Electron. Lett.,* vol. 29, pp. 1191-1193, 1993.

[32] Stephen W James and Ralph,P.Tatam, "Optical fibre long-period grating sensors: characteristics and application," *Meas. Sci. Technology,* vol. 14, pp. R49-R61, 2003.

[33] C. Nordling and J. Österman, "Solid mechanics," in *Physics Handbook for Science and Engineering*, Seventh ed.Anonymous Lund: Studentlitteratur, 2004, pp. 369.

[34] G. Meltz and W. W. Morey, "Bragg grating formation and germanosilicate fiber photosensitivity," in *Proc. SPIE 1516, International Workshop on Photoinduced Self-Organization Effects in Optical Fiber,* 1991, pp. 185-199.

[35] A. W. Sleight, "Isotropic negative thermal expansion," *Annu. Rev. Mater. Sci.,* vol. 28, pp. 29-43, 1998.

[36] S. Park, T. Park and K. Han, "Real-Time Monitoring of Composite Wind Turbine Blades Using Fiber Bragg Grating Sensors," *Adv. Compos. Mater.,* vol. 20, pp. 39-51, 2011.

[37] K. Schroder, J. Apitz, W. Ecke, E. Lembke and G. Lenschow, "Fibre bragg grating sensor system monitors operational load in a wind turbine rotor blade," in *Proc. SPIE 5855, 17th International Conference on Optical Fibre Sensors,* 2005, pp. 270-273.

[38] Z. Guo, J. Zhang, H. Hu and X. Guo, "Structural health monitoring of composite wind blades by fiber bragg grating," in *Proc. SPIE 6423, International Conference on Smart Materials and Nanotechnology in Engineering,* 2007, pp. 64230I.

[39] H. Bang, H. Shin and Y. Ju, "Structural health monitoring of a composite wind turbine blade using fiber bragg grating sensors," in *Proc. SPIE 7647, Sensors and Smart Structures Technologies for Civil, Mechanical, and Aerospace Systems,* 2010, pp. 76474H.

[40] D. L. Williams and R. P. Smith, "Accelerated Lifetime Tests on Uv Written Intracore Gratings in Boron Germania Codoped Silica Fiber," *Electron. Lett.,* vol. 31, pp. 2120-2121, 1995.

[41] H. G. Limberger, D. Varelas, R. Salathe and G. Kotrotsios, "Mechanical degradation of optical fibers induced by UV light," in *Proc. SPIE 2841, Doped Fiber Devices,* 1996, pp. 84-93.

[42] FBGS Technologies: http://www.fbgs.com/, 05/02/2014

[43] Redondo Optics: http://www.redondooptics.com/, 05/02/2014

[44] L. Glavind, I. S. Olesen, M. Thøgersen, B. F. Skipper and M. Kristensen, "Low-cost, high-resolution strain sensor for wind turbine applications," in *Bragg Gratings, Photosensitivity, and Poling in Glass Waveguides,* 2010, pp. JThA36.

[45] A. Martinez, Y. Lai, M. Dubov, I. Y. Khrushchev and I. Bennion, "Vector bending sensors based on fibre Bragg gratings inscribed by infrared femtosecond laser," *Electron. Lett.,* vol. 41, pp. 472-474, 2005.

[46] X. Chen, C. Zhang, D. J. Webb, K. Kalli and G. Peng, "Highly Sensitive Bend Sensor Based on Bragg Grating in Eccentric Core Polymer Fiber," *IEEE Photonics Technol. Lett.,* vol. 22, pp. 850-852, 2010.

[47] X. Chen, C. Zhang, D. J. Webb, R. Suo, G. D. Peng and K. Kalli, "Optical bend sensor for vector curvature measurement based on bragg grating in eccentric core polymer optical fibre," in *Proc. SPIE 7503, 20th International Conference on Optical Fibre Sensors,* 2009, pp. 750327.

[48] J. Rathje, "Thermal stability and practical applications of UV induced index changes in silica glasses," *Research Center COM, Technical University of Denmark, PhD Thesis,* 2000.

[49] V. Bhatia and A. M. Vengsarkar, "Optical fiber long-period grating sensors," *Opt. Lett.,* vol. 21, pp. 692-694, 1996.

[50] Y. Liu, L. Zhang, J. A. R. Williams and I. Bennion, "Optical bend sensor based on measurement of resonance mode splitting of long-period fiber grating," *IEEE Photonics Technol. Lett.,* vol. 12, pp. 531-533, 2000.

[51] A. M. Vengsarkar, P. J. Lemaire, J. B. Judkins, V. Bhatia, T. Erdogan and J. E. Sipe, "Long-period fiber gratings as band-rejection filters," *J. Lightwave Technol.,* vol. 14, pp. 58-65, 1996.

[52] K. O. HiIl, B. Malo, K. A. Vineberg, F. Bilodeau, D. C. Johnson and I. Skinner, "Efficient Mode Conversion in Telecommunication Fiber using Externally Written Gratings," *Electron. Lett.,* vol. 26, pp. 1270-1272, 1990.

[53] S. E. Miller and W. W. Mumford, "Multi-Element Directional Couplers," *Proceedings of the IRE,* vol. 40, pp. 1071-1078, 1952.

[54] O. V. Ivanov, S. A. Nikitov and Y. V. Gulyaev, "Cladding modes of optical fibers: properties and applications," *Physics-Uspekhi,* vol. 49, pp. 167-191, 2006.

[55] V. Bhatia, D. K. Campbell, D. Sherr, T. G. D'Alberto, N. A. Zabaronick, G. A. T. Eyck, K. A. Murphy and R. O. Claus, "Temperature-insensitive and strain-insensitive long-period grating sensors for smart structures," *Optical Engineering,* vol. 36, pp. 1872-1876, 1997.

[56] S. Savin, M. J. F. Digonnet, G. S. Kino and H. J. Shaw, "Tunable mechanically induced long-period fiber gratings," *Opt. Lett.,* vol. 25, pp. 710-712, 2000.

[57] H. S. Kim, S. H. Yun, I. K. Kwang and B. Y. Kim, "All-fiber acousto-optic tunable notch filter with electronically controllable spectral profile," *Opt. Lett.,* vol. 22, pp. 1476-1478, 1997.

[58] S. G. Kosinski and A. M. Vengsarkar, "Splicer-based long-period fiber gratings," in *Optical Fiber Communication Conference,* 1998, pp. ThG3.

[59] S. Kannan, L. Copeland, J. Judkins, M. LuValle and P. Lemaire, "Reliability of long-period gratings," in *Optical Fiber Communication Conference,* 1998, pp. 282-283.

[60] J. Jang, S. Y. Kim, S. Kim and M. Kim, "Temperature insensitive long-period fibre gratings," *Electron. Lett.,* vol. 35, pp. 2134-2136, 1999.

[61] V. Bhatia, D. Campbell, R. O. Claus and A. M. Vengsarkar. "Simultaneous strain and temperature measurement with long-period gratings". *Opt. Lett. 22(9),* pp. 648-650. 1997.

[62] Y. Liu, L. Zhang and I. Bennion, "Fibre optic load sensors with high transverse strain sensitivity based on long-period gratings in B/Ge co-doped fibre," *Electron. Lett.,* vol. 35, pp. 661-663, 1999.

[63] H. J. Patrick, C. C. Chang and S. T. Vohra, "Long period fibre gratings for structural bend sensing," *Electron. Lett.,* vol. 34, pp. 1773-1775, 1998.

[64] J. Rathje, M. Svalgaard, J. Hübner and M. Kristensen, "Sensitivity of a long-period optical fiber grating bend sensor," in *Optical Fiber Communication Conference,* 1998, pp. WM49.

[65] H. J. Patrick and S. T. Vohra, "Directional shape sensing using bend sensitivity of long period fiber gratings," in *Proc. SPIE Vol. 3746, 13th International Conference on Optical Fiber Sensors,* 1999, pp. 561.

[66] Z. H. Chen, K. S. Chiang, M. N. Ng, Y. M. Chan and H. Ke, "Bent long-period fiber gratings for sensor applications," *Advanced Photonic Sensors and Applications,* vol. 3897, pp. 94-104, 1999.

[67] C. C. Ye, C. Wei, S. Khaliq, S. W. James, P. E. Irving and R. P. Tatam, "Bend sensing in structures using long-period optical fibre gratings," in *Proc. SPIE. 4073, Fifth European Conference on Smart Structures and Materials,* 2000, pp. 311-315.

[68] J. Rathje, M. Kristensen and J. Hübner, "Effects of fiber core concentricity error and UV illumination direction on the bend direction asymmetry of long-period gratings," in *Bragg Gratings, Photosensitivity, and Poling in Glass Waveguides,* 1999, pp. BD2.

[69] Y. Liu, L. Zhang, J. A. R. Williams and I. Bennion, "Bend sensing by measuring the resonance splitting of long-period fiber gratings," *Opt. Commun.,* vol. 193, pp. 69-72, 2001.

[70] Y. Q. Liu, M. N. Ng, K. S. Chiang and J. P. Yao, "Long period fiber grating curvature sensor based on temperature-insensitive wavelength separation measurements," in *Proc. SPIE. 4596, Advanced Photonic Sensors and Applications II,* 2001, pp. 104-109.

[71] D. A. González, J. L. Arce-Diego, A. Cobo and J. M. López-Higuera, "Spectral modelling of curved long-period fibre gratings," *Meas. Sci. Technology,* vol. 12, pp. 786, 2001.

[72] U. L. Block, V. Dangui, M. J. F. Digonnet and M. M. Fejer, "Origin of apparent resonance mode splitting in bent long-period fiber gratings," *J. Lightwave Technol.,* vol. 24, pp. 1027-1034, 2006.

[73] J. Rathje and M. Kristensen, "Effects of core concentricity error on bend direction asymmetry for long-period fiber gratings," in *Bragg Gratings, Photosensitivity, and Poling in Glass Waveguides,* 1999, pp. SaC2-1 / 283.

[74] H. J. Patrick, "Self-aligning, bipolar bend transducer based on long period grating written in eccentric core fibre," *Electron. Lett.,* vol. 36, pp. 1763-1764, 2000.

[75] S. Michelsen, "Optical Fiber Grating based Sensors," *Technical University of Denmark, COM•DTU Department of Communications, Optics & Materials, Glass, PhD Thesis,* 2003.

[76] S. Søgaard, M. Kristensen and J. Rathje, "Characterization of a long-period grating (LPG) bend sensor in a core concentricity error fiber," in *Bragg Gratings, Photosensitivity, and Poling in Glass Waveguides,* 2001, pp. BTh4.

[77] D. Zhao, K. Zhou, X. Chen, L. Zhang, I. Bennion, G. Flockhart, W. N. MacPherson, J. S. Barton and J. D. C. Jones, "Implementation of vectorial bend sensors using long-period gratings UV-inscribed in special shape fibres," *Meas. Sci. Technology,* vol. 15, pp. 1647-1650, 2004.

[78] T. Allsop, A. Gillooly, V. Mezentsev, T. Earthgrowl-Gould, R. Neal, D. J. Webb and I. Bennion, "Beading and orientational characteristics of long period gratings written in D-Shaped optical fiber," *IEEE Trans. Instrum. Meas.,* vol. 53, pp. 130-135, 2004.

[79] D. Zhao, X. Chen, K. Zhou, L. Zhang, I. Bennion, W. N. MacPherson, J. S. Barton and J. D. C. Jones, "Bend Sensors with Direction Recognition Based on Long-Period Gratings Written in D-Shaped Fiber," *Appl. Opt.,* vol. 43, pp. 5425-5428, 2004.

[80] Y. N. Ning, K. T. V. Grattan, W. M. Wang and A. W. Palmer. "A systematic classification and identification of optical fibre sensors". *Sensors and Actuators A: Physical 29(1),* pp. 21-36. 1991.

[81] V. Pruneri, G. Bonfrate, P. G. Kazansky, D. J. Richardson, N. G. Broderick, J. P. d. Sandro, C. Simonneau, P. Vidakovic and J. A. Levenson, "Greater than 20%-efficient frequency doubling of 1532-nm nanosecond pulses in quasi-phase-matched germanosilicate optical fibers," *Opt. Lett.,* vol. 24, pp. 208-210, 1999.

[82] M. N. Trutzel, K. Wauer, D. Betz, L. Staudigel, O. Krumpholz, H. Muehlmann, T. Muellert and W. Gleine, "Smart sensing of aviation structures with fiber optic bragg grating sensors," in *Proc. SPIE 3986, Smart Structures and Materials,* 2000, pp. 134-143.

[83] R. Maaskant, T. Alavie, R. M. Measures, G. Tadros, S. H. Rizkalla and A. Guha-Thakurta, "Fiber-optic Bragg grating sensors for bridge monitoring," *Cement and Concrete Composites,* vol. 19, pp. 21-33, 1997.

[84] M. L. Filograno, P. Corredera Guillen, A. Rodriguez-Barrios, S. Martin-Lopez, M. Rodriguez-Plaza, A. Andres-Alguacil and M. Gonzalez-Herraez, "Real-Time Monitoring of Railway Traffic Using Fiber Bragg Grating Sensors," *Sensors Journal, IEEE,* vol. 12, pp. 85-92, 2012.

[85] M. Chomat, D. Berkova, F. Todorov, J. Ctyroky, V. Matejec, I. Kasik, J. Probostova, M. Salvia and J. Jehid, "Bend sensing with long-period fiber gratings in capillaries embedded in structures," *Mater. Sci. Eng. C-Biomimetic Supramol. Syst.,* vol. 28, pp. 716-721, 2008.

[86] J. B. MacChesney, P. B. O'Connor and H. M. Presby, "A new technique for the preparation of low-loss and graded-index optical fibers," *Proceedings of the IEEE,* vol. 62, pp. 1280-1281, 1974.

[87] S. R. Nagel, J. B. MacChesney and K. L. Walker, "An Overview of the Modified Chemical Vapor-Deposition (Mcvd) Process and Performance," *IEEE J. Quant. Electron.,* vol. 18, pp. 459-476, 1982.

[88] R. R. A. Syms and J. R. Cozens. *Optical Guided Waves and Devices*. McGraw-Hill Ryerson, 1992.

[89] I. H. Malitson, "Interspecimen Comparison of the Refractive Index of Fused Silica," *J. Opt. Soc. Am.,* vol. 55, pp. 1205-1208, 1965.

[90] A. Ghatak and K. Thyagarajan, *An Introduction to Fiber Optics.* Cambridge University Press, 1998.

[91] L. Glavind, J. Canning, S. Gao, K. Cook, G. D. Peng, Y. Luo, B. F. Skipper and M. Kristensen, "Long-Period Gratings in Special Geometry Fibres for High Resolution and Selective Sensors," *Optical Engineering,* submitted Jan. 2014.

[92] L. Moura, J. Canning, L. Lindoy, K. Cook, M. Crossley, Y. Luo, G. Peng, L. Glavind and M. Kristensen, "A fluorescence study of self-assembled silica layers on D-shaped optical fibre," in *Asia Pacific Optical Sensors Conference 2013,* 2013, pp. 89241V.

[93] J. Canning, L. Lindoy, G. Huyang, M. Naqshbandi, K. Cook, M. J. Crossley, Y. Luo, G. Peng, L. Glavind and M. Kristensen, "Exploring the room temperature self-assembly of silica nanoparticle layers on optical fibres," in *Fourth International Conference on Smart Materials and Nanotechnology in Engineering,* 2013, pp. 87930J.

[94] Canning, John and Lindoy, Lachlan and Huyang, George and Naqshbandi, Masood and Cook, Kevin and Crossley, Maxwell and Luo, Yanhua and Peng, Gang-Ding and Glavind, Lars and Town, Graham and others, "RT self-assembly of silica nanoparticles on optical fibres," in *Workshop on Specialty Optical Fibers and their Applications,* 2013, pp. F2-3.

[95] N. F. Ramsey, *Molecular Beams.* University Press, 1956.

[96] E. Dianov, S. Vasiliev, A. Kurkov, O. Medvedkov and V. Protopopov. "In-fiber mach-zehnder interferometer based on a pair of long-period gratings". In *22nd European Conference on Optical Communication.* 1996, pp. 65-68.

[97] D. Stegall and T. Erdogan. "Leaky cladding mode propagation in long-period fiber grating devices". *IEEE Photonics Technol. Lett. 11(3),* pp. 343-345. 1999.

[98] Z. Tian, S. S. -. Yam, J. Barnes, W. Bock, P. Greig, J. M. Fraser, H. Loock and R. D. Oleschuk, "Refractive index sensing with Mach-Zehnder interferometer

based on concatenating two single-mode fiber tapers," *IEEE Photonics Technol. Lett.,* vol. 20, pp. 626-628, 2008.

[99] T. Allsop, R. Reeves, D. Webb, I. Bennion and R. Neal, "A high sensitivity refractometer based upon a long period grating Mach-Zehnder interferometer," *Rev. Sci. Instrum.,* vol. 73, pp. 1702-1705, 2002.

[100] S. J. Buggy, R. P. Murphy, S. W. James and R. P. Tatam. "Cure monitoring of a UV cured epoxy resin using a long period grating mach-zehnder interferometer". *Proc. SPIE. 6619, Third European Workshop on Optical Fibre Sensors.* 2007, 66190V.

[101] B. H. Lee and J. Nishii, "Bending sensitivity of in-series long-period fiber gratings," *Opt. Lett.,* vol. 23, pp. 1624-1626, 1998.

[102] D. Marcuse. "Directional-couplers made of nonidentical asymmetric slabs .2. grating-assisted couplers". *J. Lightwave Technol. 5(2),* pp. 268-273. 1987.

[103] Y. Tan, L. Sun, L. Jin, J. Li and B. Guan, "Microfiber Mach-Zehnder interferometer based on long period grating for sensing applications," *Opt.Express,* vol. 21, pp. 154-164, 2013.

[104] L. Glavind, S. Gao, K. Cook, J. Canning, B. Skipper, Y. Luo, G. Peng and M. Kristensen, "Enhanced resolution of long-period grating bend sensor," in *Asia Pacific Optical Sensors Conference 2013,* 2013, pp. 892437.

[105] T. Kubo, B. Malinsky, Y. Kanda and W. Zheng, "Automated Fusion Splicing of Circular and D-shaped Fiber with Elliptical Core," *Fujikura Technical Review,* vol. 39, pp. 22-26, 2010.

[106] Performance Composites: http://www.performancecomposites.com/about-composites-technical-info/124-designing-with-carbon-fiber.html, 05/02/2014

[107] K. Studer, C. Decker, E. Beck and R. Schwalm, "Overcoming oxygen inhibition in UV-curing of acrylate coatings by carbon dioxide inerting, Part I," *Progress in Organic Coatings,* vol. 48, pp. 92-100, 2003.

[108] L. Glavind, S. Buggy, I. S. Olesen, B. F. Skipper, J. Canning, K. Cook and M. Kristensen, "Direct embedding of fiber-optical load sensors into wind turbine blades," in *Optical Sensors,* 2013, pp. SM3-6.

[109] Vytran: http://www.vytran.com/product/ptr-200_series, 05/02/2014

[110] N. Skivesen, A. Tetu, M. Kristensen, J. Kjems, L. H. Frandsen and P. I. Borel. "Photonic-crystal waveguide biosensor". *Opt. Express 15(6),* pp. 3169-3176. 2007.

[111] W. Du, H. Tam, M. S. Y. Liu and X. Tao. Long-period fiber grating bending sensors in laminated composite structures. Presented at Proc. SPIE 3330, Smart Structures and Materials. 1998, .

[112] D. Marcuse, F. Ladouceur and J. D. Love. Vector modes of D-shaped fibers. *IEE Proceedings J. Optoelectronics 139(2),* pp. 117-126. 1992.

[113] L. Glavind, S. Buggy, B. F. Skipper, J. Canning, S. Gao, K. Cook, Y. Luo, G. Peng and M. Kristensen, "A long-period grating sensor system monitoring loads on a wind turbine blade," in *Bragg Gratings, Photosensitivity and Poling in Glass Waveguides,* Submitted Jan. 2014, .

[114] L. Glavind, J. Canning, S. Gao, K. Cook, G. Peng, Y. Luo, B. F. Skipper and M. Kristensen, "D-shape fiber with mach zehnder long-period gratings for a high resolution and selective sensor," in *Bragg Gratings, Photosensitivity and Poling in Glass Waveguides,* Submitted Jan. 2014, .

[115] J. Canning, M. Kristensen and K. Cook, "Wavelength-selective mode-switching in a reflective long period grating mach-zehnder interferometer," in *Advanced Photonics Congress,* 2012, pp. BTu1.1.

# 7. Appendix A

"Long-Period Gratings in Special Geometry Fibres for High Resolution and Selective Sensors" [91, 114].

Utilizations of the general principle of interaction between a particle and two consecutive oscillatory fields, developed originally by Ramsey [95], provide narrow resonances for high-resolution detection of the sensing parameter and reduce noise [95]. This has been demonstrated in special fibers with and without access along the fiber to the surroundings provides devices for a large number of applications. Here identical LPGs in an optical fiber act as a MZ device in transmission [96]. This principle has been demonstrated for various sensing applications such as refractive index and bends sensing [98, 99, 104].

Two identical LPGs were written in an inner cladding optical fiber, see RI profile in figure 77, acting as a MZ device in transmission [115], see figure 78.

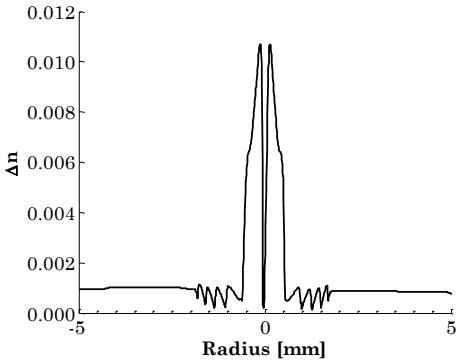


Figure 77 – Index profile of preform for inner cladding fibre, from [91]

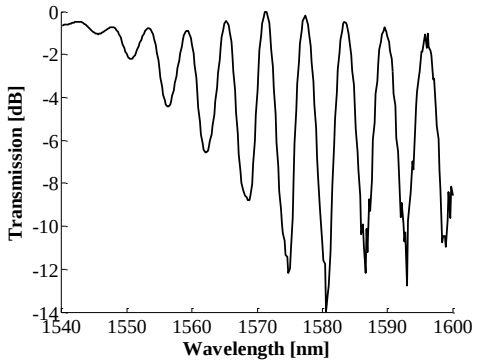


Figure 78 – Normalized spectrum of the MZ configuration in inner cladding fibre, from [91]

Such fiber where cladding modes are confined in the inner cladding of a fiber provides a very robust device which is immune to the sounding along the fiber, whilst enabling a highly sensitive interference device for sensing at the fiber end where the fiber is cleaved. This can give a compact and cheap device that can provide switching between different mode patterns. By sweeping the wavelength to tune the phase rather than mechanically moving a cavity, modulation becomes passive (i.e. no moving parts) and faster resulting in improved noise suppression and longer term operation.

Figure 79 and 80 shows the mode-profile, for the inner cladding fibre, at constructive interference between the core and cladding modes corresponding to maximum back-reflection at 1577.4 nm, and with destructive interference and minimum back reflection at 1580.6 nm. The wavelength-shift between exciting predominantly the core and cladding modes is about 3.2 nm (simulated distance 2.8 nm). This can easily be tuned for a given application as it is proportional to the effective separation between the gratings.

On the other hand, the D-shape fiber used for blade load sensing, can provide a device with the opposite properties as it can be highly sensitive to changes in the surroundings along the fiber. The model in chapter 4.2 describes that with the right design (selection of TE-TM_like coupling), the sensor can be extremely sensitive. In the D-shape fiber, both the core- and cladding-mode are close to the surroundings at the flat-side, and thereby both modes utilized by the LPG are affected by the surrounding index. This is different from the inner cladding fiber, where neither core nor cladding modes used by a LPG are affected, and conventional fiber LPGs where the core mode is not affected although the cladding mode will be. This provides the possibility of measurement using both modes, and utilizing one as internal reference, potentially reducing noise and providing improved spectral resolution. The D-shape fiber sensor is particularly suitable for a chemical or biological sensor, for example.

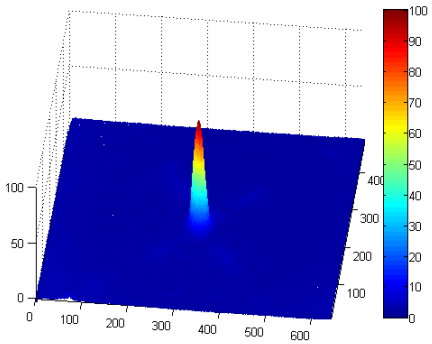


Figure 79 –Normalized core mode-profile-intensity-pattern in transmission at 1577.4 nm, from [91]

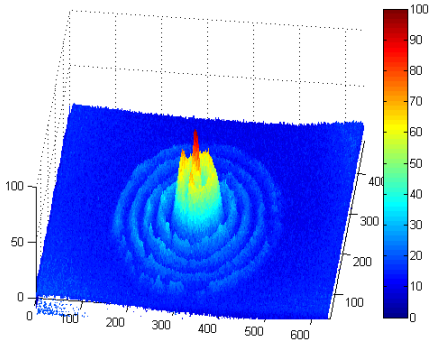


Figure 80 – Normalized cladding-mode-profile intensity-pattern in transmission at 1580.6 nm, from [91]